Ore Geology Reviews 101 (2018) 1–16

Contents lists available at ScienceDirect

Ore Geology Reviews

journal homepage: www.elsevier.com/locate/oregeorev

A magmatic-hydrothermal origin for Ag-Pb-Zn vein formation at the Bianjiadayuan deposit, inner Mongolia, NE China: Evidences from fluid inclusion, stable (C-H-O) and noble gas isotope studies

Degao Zhai[a,b,*], Jiajun Liu[a], Hongyu Zhang[a], Stylianos Tombros[c], Anli Zhang[d]

[a] State Key Laboratory of Geological Processes and Mineral Resources, China University of Geosciences, Beijing 100083, China
[b] Department of Earth and Planetary Sciences, McGill University, 3450 Quebec, Canada
[c] Department of Geology, University of Patras, Rion, 26500 Patras, Greece
[d] Lituo Mining Company, Chifeng 024000, China

ARTICLE INFO

Keywords:
D-O-C isotopes
Noble gas isotopes
Ag-Pb-Zn veins
Bianjiadayuan
NE China

ABSTRACT

Many new discoveries of base and precious metal veins in the Great Hinggan Range district have made this region the most important Ag-Pb-Zn metallogenic belt in northern China. The Bianjiadayuan Ag-Pb-Zn deposit (4.81 Mt @157 g/t Ag and 3.94% Pb + Zn) is one of the new discoveries located in the southern segment of this potentially important but poorly understood metallogenic belt. Vein-type Ag-Pb-Zn ore bodies are predominantly hosted by slate adjacent to a Sn ± Cu ± Mo mineralized porphyry intrusion. Four primary ore stages of arsenopyrite + pyrite + quartz, main sulfides + quartz, silver-bearing sulfosalts + quartz, and boulangerite + calcite are recognized, and a subsequent supergene oxidation stage has also been identified. An alteration assemblage of quartz, sericite, chlorite and epidote is spatially associated with this vein type mineralization. The δD_{H2O} (−139 to −106‰) and $\delta^{18}O_{H2O}$ (−16.4 to 12.1‰) isotope compositions obtained from different stage vein quartz and calcite reveal that the early stage ore fluids were dominated by magmatic fluids, whereas the late stage ore fluids contained a significant proportion of meteoric waters, which is consistent with the $\delta^{13}C_{PDB}$ (−7.7 to −2.7‰) and $\delta^{18}O_{SMOW}$ (−0.4 to 6.4‰) isotope signatures for waning stage calcites reflecting an addition of large volumes of meteoric waters in hydrothermal system. Noble gas isotopes (i.e., $^3He/^4He$ ratios of 1.52–3.06 Ra) display evidences of a magmatic fluid responsible for ore formation in the deposit. Fluid inclusion studies suggest that vein formation occurred at progressively lower temperature (310–220 °C) and pressure (100–20 bars). Fluid cooling, phase separation, and mixing with meteoric waters are advocated as the important factors for ore deposition. In combination, available data for the Bianjiadayuan deposit suggest that local Ag-Pb-Zn veins and porphyry type Sn ± Cu ± Mo mineralization are genetically related and formed in one porphyry ore system, which is a useful concept for local and regional Ag-Pb-Zn exploration.

1. Introduction

Available geological and geochemical studies reveal that numerous base metal veins are genetically related to the porphyry Cu-Mo mineralization (Hedenquist et al., 1998; Muntean and Einaudi, 2000; Heinrich, 2005; Sillitoe, 2010; Sillitoe and Mortensen, 2010). A close spatial and temporal relationship between porphyry Cu-Mo and polymetallic vein mineralization has been well documented in many ore districts worldwide, e.g., the Main Stage veins at Butte, USA (Reed et al., 2013), the Cu-Mo ± Re ± Au mineralization at Pagoni Rachi/Kirki in northern Greece (Voudouris et al., 2013), and the base metal veins at Morococha, Peru (Catchpole et al., 2015). In these ore districts, base metal mineralization typically occurs peripheral to, adjacent to, or superimposed on the mineralized porphyry systems (Seedorff et al., 2005; Sillitoe, 2010; Catchpole et al., 2015; Melfos and Voudouris, 2017; Rottier et al., 2018). However, there are also some base metal veins that do not appear to be genetically linked to porphyry deposits and their genesis remains controversial. Such vein-type deposits are obviously hydrothermal in origin, although the source of ore-forming fluids and metals may be either magmatic or non-magmatic. In many cases, both fluid sources and deposition processes of metals from the hydrothermal solutions are still greatly debated (Kissin and Mango,

* Corresponding author at: State Key Laboratory of Geological Processes and Mineral Resources, China University of Geosciences, Beijing 100083, China.
E-mail address: dgzhai@cugb.edu.cn (D. Zhai).

https://doi.org/10.1016/j.oregeorev.2018.07.005
Received 13 March 2018; Received in revised form 4 July 2018; Accepted 11 July 2018
Available online 12 July 2018
0169-1368/

2014).

The Great Hinggan Range (GHR) metallogenic belt in NE China hosts a number of porphyry Mo(Cu), skarn Fe(Sn), epithermal Au-Ag and hydrothermal vein type Ag-Pb-Zn ore deposits (i.e., Zeng et al., 2011, 2015; Zhai and Liu, 2014; Zhang and Li, 2014, 2017; Shu et al., 2016; Zhai et al., 2014a, b, c, 2015; Chen et al., 2017; Gao et al., 2017). Recent ore exploration and targeting have successfully discovered numerous Ag-Pb-Zn vein type deposits in the southern segment of the GHR (i.e., Ouyang et al., 2014, 2015; Ruan et al., 2015; Liu et al., 2016a; Liu et al., 2016c; Wang et al., 2017), defining a new important Ag-Pb-Zn metallogenic belt in NE China. One of the significant new discoveries is the Bianjiadayuan deposit, which has reserves > 4.8 Mt grading 157 g/t Ag and 3.94% (Pb + Zn). Recent drilling and mining have identified new porphyry type Sn ± Cu ± Mo mineralization adjacent to Ag-Pb-Zn veins in the Bianjiadayuan ore district. A close genetic relationship between porphyry and base metal vein type mineralization has been recently suggested for some ore deposits in the southern GHR district, i.e., the Weilasituo porphyry Sn-W-(Rb) and Cu-Zn-Ag vein type mineralization (Wang et al., 2017). Although a close spatial association has been identified between the porphyry Sn ± Cu ± Mo mineralization and Ag-Pb-Zn veins at the Bianjiadayuan, whether these two different type ores are genetically related is yet unknown.

In the current contribution, we report the results of a comprehensive study of the Bianjiadayuan Ag-Pb-Zn deposit that makes use of fluid inclusion and isotopic analyses (O, H, C, He and Ar) to determine the source, nature and evolution of the ore fluid, and the key controls on ore mineral precipitation. Using these data with a combination of available geological, S-Pb isotope and geochronological investigations, we propose a genetic model for ore formation at Bianjiadayuan ore district suggesting that local Ag-Pb-Zn veins are genetically related to the adjacent Sn ± Cu ± Mo mineralized porphyry intrusion. This is useful for local and regional Ag-Pb-Zn ore exploration.

2. Regional geological setting

The Bianjidayuan Ag-Pb-Zn deposit occurs in the GHR metallogenic belt, which lies in the easternmost part of the Central Asian Orogenic Belt (CAOB, Fig. 1a). The CAOB developed during the Neoproterozoic to Phanerozoic, and is rimmed by the Siberian, Tarim and North China Cratons (Fig. 1a). It formed via successive accretion of arc complexes, accompanied by emplacement of immense volumes of granitic magmas (Jahn et al., 2000). The CAOB contains a wide range of tectonic elements that include microcontinents, arc-back arc systems, oceanic islands/plateaus, ophiolites, and subduction-accretion complexes (Zhou et al., 2017).

The region is characterized by widespread Mesozoic volcanic and intrusive rocks (Fig. 1b), including I- and A-type granitoids (Wu et al., 2005, 2011), which comprise > 50% of the surface area in the mountainous regions according to regional geological surveys (HBGMR, 1993). Those granitoids in the CAOB constitute one of the largest plutonic provinces in the world and one of the most important sites of juvenile crust formation during the Phanerozoic (Wu et al., 2011). Based on a large dataset and a precise geochronological framework for the regional intrusion ages, these volcanics and granitoids have been broadly divided into two groups, which were emplaced in two geotectonic episodes. The first group belongs to a Permian and Triassic episode (275–210 Ma, zircon U-Pb method), whereas the second group is Jurassic to Cretaceous in age (160–130 Ma, zircon U-Pb method) (Wu et al., 2004; Wei et al., 2008; Zhang et al., 2010). The first group is mainly composed of calc-alkaline I- and S-type plutons; the latter are products of post-orogenic extension. During the Late Jurassic, collision was succeeded by subduction of the Paleo-Pacific plate beneath the Eurasian continental plate, in response to crustal thickening. Available Sr-Nd isotope data suggest that these magmas were derived from asthenospheric mantle and recycled ancient crust (Chen and Jahn, 2001). The second group comprises both I-type (granodiorite, monzogranite and syenite) and A-type granitoid plutons, which were emplaced within NNE to NE trending extensional fault zones and formed from melts derived from the lower crust (Wei et al., 2008). In detail, the regional Cretaceous granitoids show an eastwards-younging trend, which indicates their emplacement in an extensional setting (Wu et al., 2003). It is proposed that early Paleo-Pacific subduction in the Jurassic caused subsequent lithospheric delamination or rollback and extension of the back-arc area, successively enabling emplacement of Cretaceous granitoids (Wang et al., 2006; Zhang et al., 2008, 2010). Compared with other areas in the CAOB, NE China was significantly affected by the Paleo-Pacific subduction (Wu et al., 2011).

The southern segment of the GHR Metallogenic Belt hosts many porphyry Mo(Cu), skarn Fe-Sn, and epithermal and hydrothermal polymetallic (Ag-Pb-Zn-Cu) vein-type ore deposits (Fig. 1c, Zhai et al., 2014b, 2018a). Recent ore exploration revealed that Ag-Pb-Zn-(Cu) vein type deposits are particularly common in the southern segment of the GHR (Fig. 1c), leading to new discoveries of the Shuangjianzishan, Bianjiadayuan, Bairendaba and Weilasituo deposits (Ouyang et al., 2014; Ruan et al., 2015; Liu et al., 2016c; Wang et al., 2017). Those discoveries have defined an important Ag-Pb-Zn polymetallic metallogenic belt in NE China. The discovered ore deposits in this district are mostly related to Jurassic to Cretaceous magmatism (Mao et al., 2005; Chen et al., 2007; Zhai et al., 2014b). Regionally, mineralization and Jurassic to Cretaceous granites demonstrate a close spatial distribution (Fig. 1c). Spatial distributions of the regional deposits are predominantly associated with a zone of NE-trending normal faults that is about 100-km-long and 20-km-wide (Fig. 1c, Ouyang et al., 2015).

Available geochronological data reveal that magmatic-hydrothermal deposits in the area formed during two distinct metallogenic events (Li et al., 2012): an early event in the Late Permian (272 ± 3–256 ± 7 Ma, zircon U-Pb and molybdenite Re-Os); and a later event in the Cretaceous and Jurassic (167 ± 2–129 ± 3 Ma, zircon U-Pb, molybdenite Re-Os and sericite ^{40}Ar-^{39}Ar). Most porphyry Mo(Cu) and skarn Fe-Sn deposits formed during the second metallogenic event, associated with intrusion of A-type granites (Mao et al., 2005; Wu et al., 2005, 2011; Zhai et al., 2018a); whereas precise ages for Ag-Pb-Zn mineralization in the area are largely lacking.

3. Ore deposit geology

The strata exposed in the ore district mainly involve the Permian Zhesi Formation, comprising slates and siltstones that dip to NNW at 50–55°, and Quaternary alluvial deposits (Fig. 2a). The identified Ag-Pb-Zn veins are predominantly hosted by the Permian slate. The dominant igneous rocks exposed in the ore district are gabbro, quartz porphyry, and numerous NE- and NW-trending granite dikes (Fig. 2a). The gabbro pluton (strike of 300°) accounts for > 20% of the surface outcrop in the mine area, with a length of 1 km and a width of ~300 m (Fig. 2a). It displays a typical gabbroic texture and is mainly composed of plagioclase (~55–60%), pyroxene (~30%), hornblende (~5%) and biotite (~5%) (Wang et al., 2013). Zircon U-Pb ages for the gabbro are 133.0 ± 0.8 and 133.2 ± 0.9 Ma (Wang et al., 2013; Zhai et al., 2017). Several base metal (Cu-Pb-Zn) veins are hosted by the gabbro (Fig. 2a). Quartz porphyry is mostly concealed in the western part of the ore district with a small occurrence in the southeast (Fig. 2a). Recent core drilling identified that the porphyry from the western part occupies an area with a length of 1500 m and a width of 270–750 m, and the area of the mineralized part is approximately 0.7 km^2. These rocks consist of quartz (~45–50%), K-feldspar (~40–45%), plagioclase (~5–10%) and minor biotite. Zircon U-Pb ages for the quartz porphyry range from 140.8 ± 0.9 to 140.2 ± 0.6 Ma (Zhai et al., 2017). Recent core drilling and exploration has identified new porphyry type Sn ± Cu ± Mo and breccia type Sn-Pb-Zn zones in west of the Ag-Pb-Zn veins in the Bianjiadayuan ore district (Fig. 2a). Porphyry type mineralization is commonly centered over, around and on the top of the concealed porphyry intrusion. The Sn ± Cu ± Mo mineralized zones

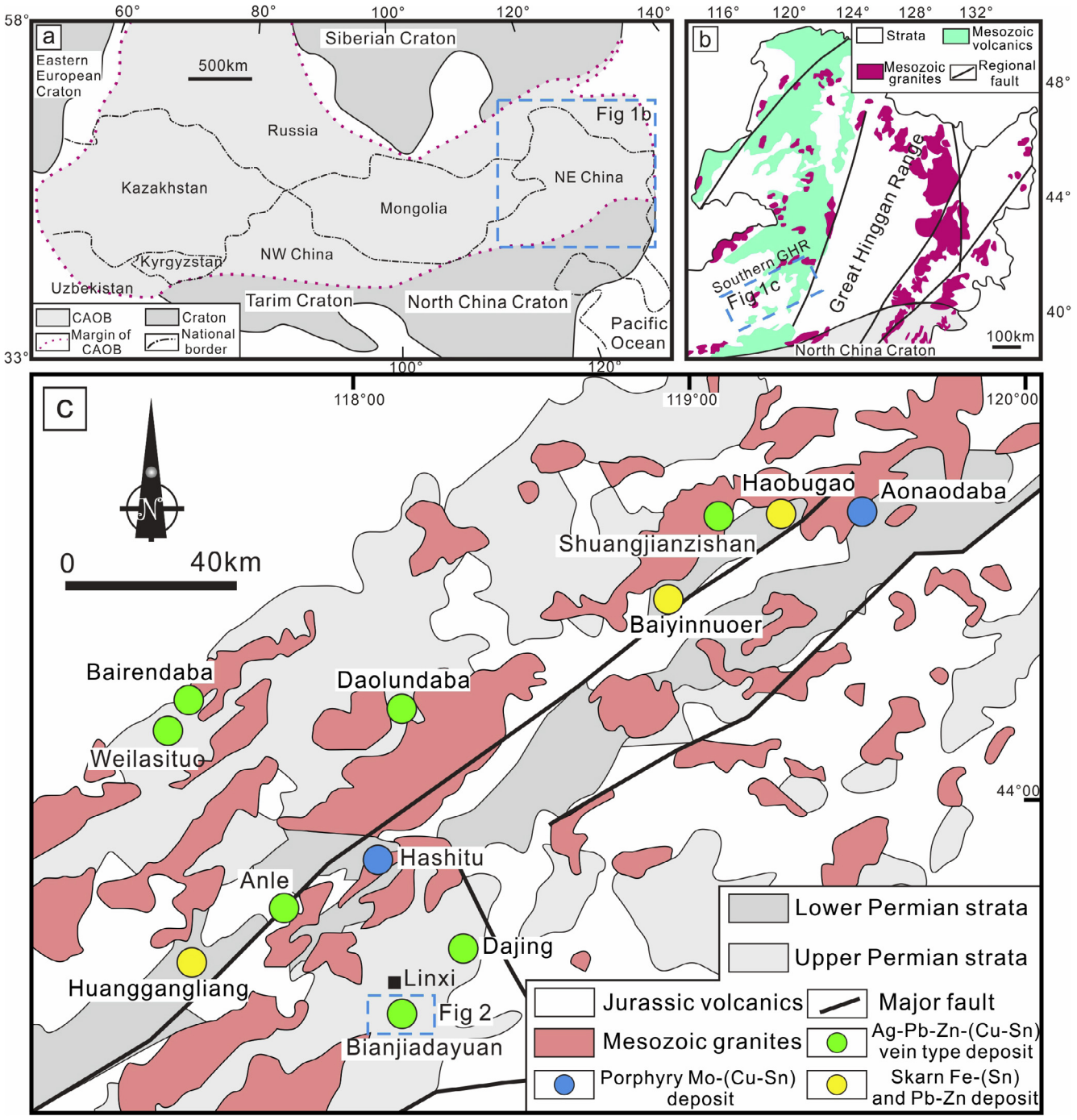

Fig. 1. (a) Tectonic scheme of the Central Asian Orogenic Belt (CAOB, modified from Jahn et al., 2000); (b) Geological map of the Great Hinggan Range (GHR) in NE China showing the distribution of the Mesozoic granites and volcanics (modified from Zhai et al., 2015); (c) Geological map of the southern GHR showing the locations of major ore deposits (modified from Zhai et al., 2018a).

are dominantly structurally controlled, with most occurring as veins, stockworks, veinlets and disseminations in altered porphyry. The ore metals display a zonation of Sn, Cu, and Mo in vertical direction from the porphyry core upwards. The porphyry type ores comprise of cassiterite, stannite, pyrite, and minor molybdenite, chalcopyrite, pyrrhotite. The breccia is spatially related to the quartz porphyry intrusion, and dominantly comprises fragments of slate and quartz porphyry with a cement mainly composed of fine rock fragments and sulfides. Formation of the breccia was considered to relate to the concealed quartz porphyry (Wang et al., 2014). Until now, these porphyry and breccia type ores have not been mined. Numerous N-E- and rare N-S-trending granitic sills and dikes intruded Permian slate and the main gabbro body (Fig. 2a). These dikes have variable widths up to 10 m, and U-Pb zircon ages between 129.7 ± 0.4 and 130.0 ± 2.8 Ma (Wang et al., 2013; Zhai et al., 2017).

Recent ore exploration in the southern segment of the GHR region has revealed that Sn mineralization is relatively common, which has led to several new discoveries including the Weilasituo greisen/porphyry and the Bianjiadayuan porphyry Sn deposits. With combination of previously identified Sn deposits, e.g., the Huangganglian skarn Fe-Sn and the Anle vein type Cu-Sn deposits, this regions is a potentially important Sn ore district. The Bianjiadayuan porphyry Sn mineralization is similar in many respects to the regional magmatic-hydrothermal Sn deposits, these include: (1) they all form in late Mesozoic (e.g.,

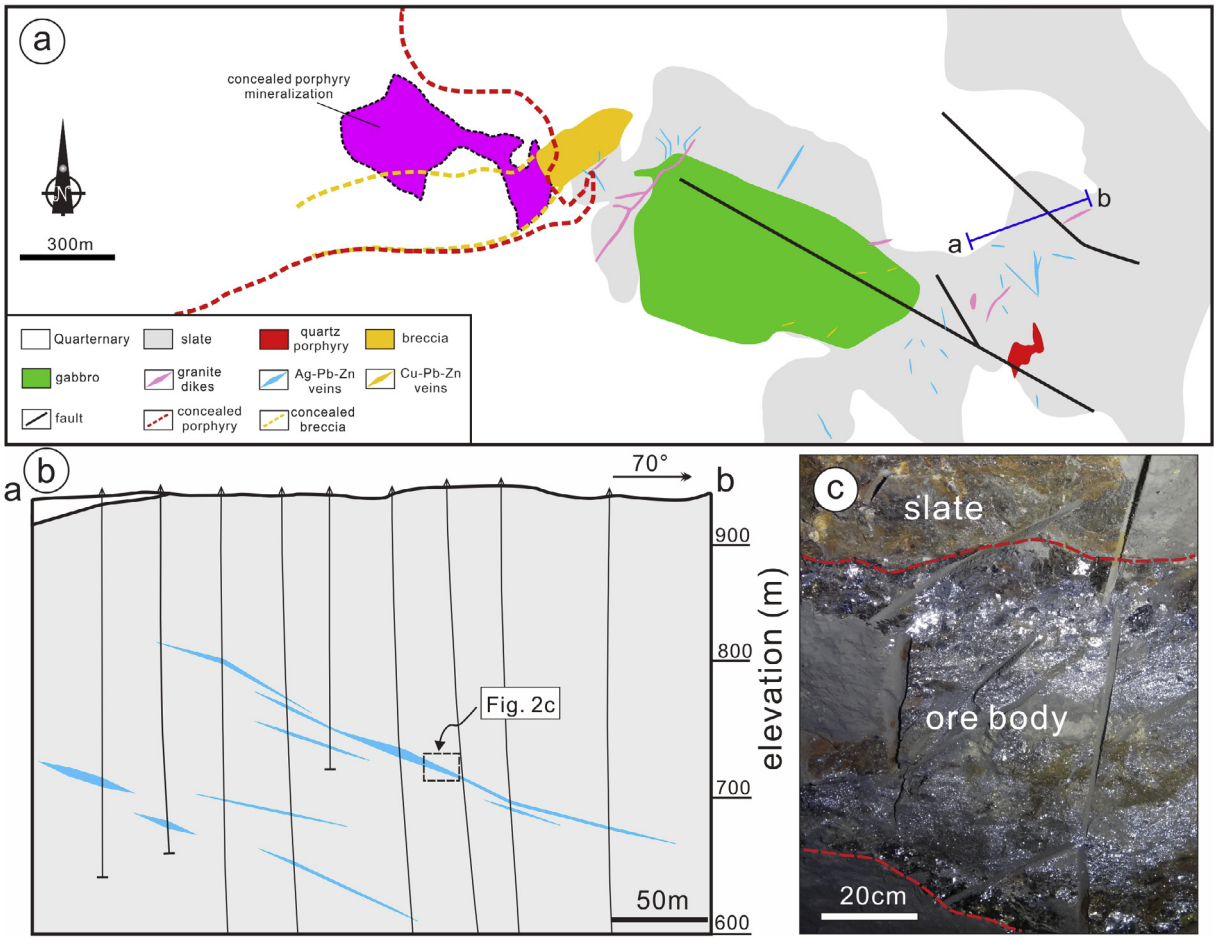

Fig. 2. Simplified geologic map (a) and representative cross-sections (b) showing the distribution of igneous rocks and vein type mineralization at Bianjiadayuan ore district (modified from Zhai et al., 2017); (c) occurrence of vein type ore body hosted by slate.

140–135 Ma), (2) many of them show a well-developed metal zonation in ore deposit scale (e.g., Sn ± Cu ± Mo to Ag-Pb-Zn), (3) they have the close spatial, temporal and genetic relationship with felsic intrusions originated from the lower crust in an extensional setting (Mao et al., 2005; Ouyang et al., 2015; Zhai et al., 2017; Wang et al., 2017). Tin is commonly concentrated in the continental crust and forms deposits hosted by continentally-derived reducing granitoids. In the southern segment of the GHR, the local Sn enrichment was considered to be introduced from reducing granitic intrusions that were the product of melting of the continental crust by mafic mantle magma during a period of slab-roll-back extension (Zhai et al., 2017).

Regionally, the emplacement of igneous rocks appears primarily controlled by NE-NNE-oriented faults (Fig. 1c). However, within the ore district, the Bianjiadayuan Ag-Pb-Zn veins are structurally controlled by NW-oriented brittle faults (Fig. 2a). Those faults and fractures typically have lengths of 220–600 m, and widths up to 10 m with dip angles of 65–80°. Open faults and fractures are the most favorable structures for Ag-Pb-Zn veins. The major faults crosscut the Permian slate, as well as the gabbro and quartz porphyry (Fig. 2a). Silicification, calcitization and chloritization are observed along the margins of the major faults and fractures.

4. Mineralization, paragenesis and alteration

Mineralized Ag-Pb-Zn veins in the Bianjiadayuan ore deposit were discovered in 2012 and then mined. More than 20 major veins, numerous stockworks, as well as minor disseminations have been identified during mine-scale exploration, which are principally hosted in the Permian slate located at least several hundred meters east of the porphyry Sn ± Cu ± Mo mineralized zones (Fig. 2a). The Ag-Pb-Zn mineralization is mainly hosted by NW- and NE-trending open-space filling veins characterized with a length from 50 to ~200 m, and extend vertically at least as much as 300 m (Fig. 2b). Their maximum widths vary from 25 to ~50 m, with an average of ~9 m. The mineralized veins are gently-dipping (25-45°) in horizontal and vertical profiles (Fig. 2c), although some dip more steeply (~75°). Numerous stockworks, veinlets and disseminations occur on the margins of the major veins in the altered slate (Fig. 3a). Some shallow mineralized veins are oxidized at outcrop, providing a valuable guide for underground exploration.

Over twenty ore and gangue minerals have been identified in four primary paragenetic stages (I–IV), and a subsequent supergene oxidation stage (V), based on the nature of the mineralization and prevailing mineral assemblages (Fig. 4). Paragenetic stages progressively demonstrate element associations changing from Fe-As-S, through Pb-Zn-Fe-Cu-S and Ag-Pb-Zn-Sb-S, to Pb-Sb-S. In detail, ore stage I is dominated by arsenopyrite and pyrite coexisting with quartz. Stage II is the main paragenetic stage for sulfide mineralization. The sulfide minerals in this stage dominantly comprise intergrowths of galena, sphalerite, pyrrhotite, pyrite and chalcopyrite (Fig. 3b, c). Overall, the stage II veins are sulfide-dominant, resulting in massive ores within the largest veins (Fig. 3a). The sulfides are commonly replaced by late-stage minerals, notably sulfosalts including freibergite (Fig. 3d) and boulangerite. In hypogene stage III, the ore mineral assemblage is dominated by silver-bearing sulfosalts, i.e., freibergite, pyrargyrite and boulangerite. High grade silver-rich ores with Ag grades up to 3000 g/t have been

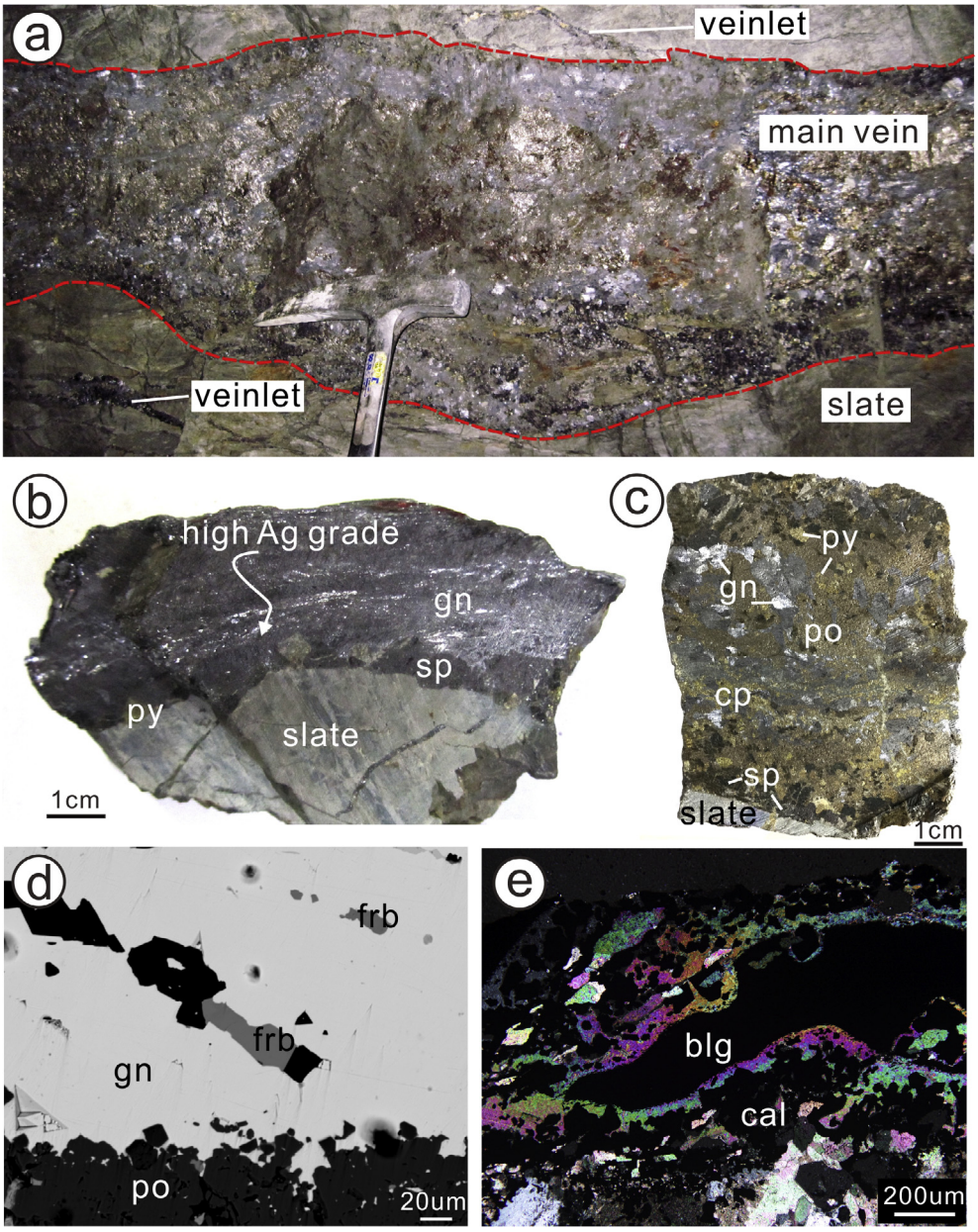

Fig. 3. Vein type ore body occurrence and ore textures for the Bianjiadayuan Ag-Pb-Zn mineralization. (a) Spatial relationship between main Ag-Pb-Zn vein and veinlets hosted in the altered slate; (b) High Ag grade vein type ore; (c) Massive Ag-Pb-Zn ore; (d) Freibergite intergrown with galena (back-scatter electron image); (e) Boulangerite coexisting with calcite in late stage vein (crossed polarized transmitted light). Abbreviations: cal-calcite; cp-chalcopyrite; blg-boulangerite; frb-freibergite; gn-galena; po-pyrrhotite; py-pyrite; sp-sphalerite.

identified in the deposit (Fig. 3b). Freibergite is the most abundant and widely distributed Ag-bearing sulfosalt in the deposit (Fig. 3d), making up approximately 90 vol% of the total Ag-bearing ore minerals. The final stage IV contains only boulangerite coexisting with calcite (Fig. 3e). This mineral assemblage occurs as late veins cutting all previous assemblages. Supergene minerals include anglesite ($PbSO_4$), malachite and limonite, which formed owing to the oxidation of primary sulfides.

Hydrothermal alteration is widespread at Bianjiadayuan, and the alteration halos are distributed asymmetrically on either side of the mineralized veins, and are typically widest around the thickest veins as discontinuous borders and envelopes. Distinct episodes of alteration assemblages are described as follows. Silicification is the most widespread expression of alteration type in the deposit, as fine silica within silicified slate. Silicification predated the main sulfide mineralization and coexists with stage I sulfides, which were successively followed by an alteration assemblage of quartz, chlorite, epidote, and minor sericite and fluorite. This alteration is spatially associated with the main sulfide assemblage. Both above alteration assemblages were further overprinted by an alteration assemblage of quartz, sericite, and subordinate chlorite and epidote, which appears closely related to local silver mineralization. The final stage alteration is characterized by an assemblage of illite and calcite, which overprinted all previous alteration types and occurs predominately along fractures. There is no apparent spatial zonation of alteration types as, in most places, alteration assemblages are superimposed upon one another.

The alteration types and zonation associated with porphyry type Sn ± Cu ± Mo mineralization are very similar to those of other typical porphyry Cu-Mo deposits worldwide. The core of the porphyry system experienced an early weak potassic alteration, which is manifested by the presence of secondary K-feldspar and biotite. Outwards and above the potassic alteration zone, phyllic alteration is the most

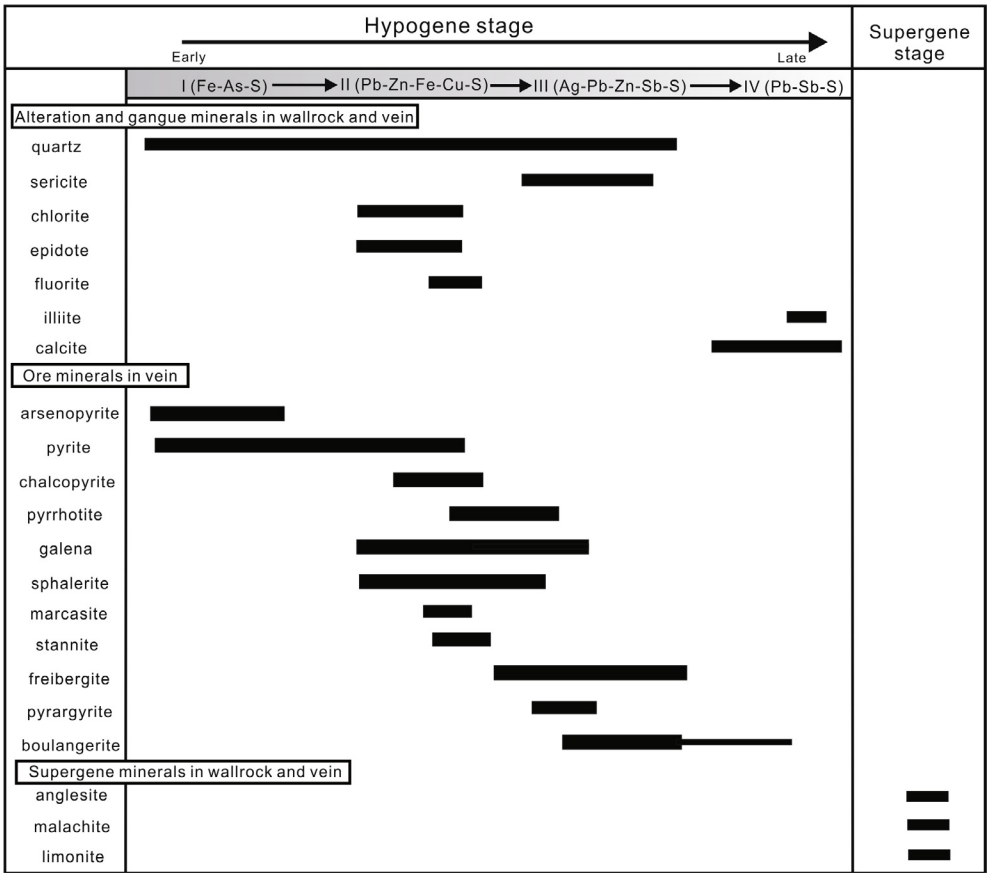

Fig. 4. Summary of paragenetic stages for the Bianjiadayuan Ag-Pb-Zn mineralization.

widespread alteration type, which is characterized by an alteration assemblage of secondary quartz, sericite and disseminated or veinlet pyrite. Finally, propylitic alteration forms a halo to the porphyry system, which is documented by the occurrence of abundant chlorite and epidote with subordinate quartz and carbonate.

5. Sampling and analytical methods

More than 50 samples were collected from different mining levels (+170 to +50 m). Ore-bearing quartz and calcite from different stages were collected for fluid inclusion studies and stable isotope (D-C-O) measurements, and sulfides from the main ore stage were separated for He-Ar isotope studies. All minerals selected for isotope studies were handpicked and checked under a binocular microscope to ensure a purity of > 98%.

Prior to microthermometric studies, the internal zoning of quartz was examined using a cathodoluminescent (CL) spectrometer (Garton Mono CL3+) equipped on a Quanta 200F ESEM with 45-s scanning time at conditions of 15 kV and 120 nA at Peking University. Microthermometric measurements of fluid inclusions were performed on a LINKAM MDSG600 heating-freezing stage coupled to a ZEISS microscope in the School of Earth Sciences and Resources, China University of Geosciences Beijing (CUGB). Most analyzed quartz crystals were directly in contact with sulfides. The temperature range for the analysis was from -196 to +600 °C. Measurements were accurate to within ± 0.1 °C and freezing-heating rates were maintained at between 0.2 and 5 °C/min. However, when approaching a phase transition the rate was dropped to 0.1–0.5 °C/min. Microthermometric data were reduced using FLINCOR software (Brown 1989), and the results are summarized in Table 1. Fluid inclusion laser Raman spectroscopy analysis was carried out in the Beijing Research Institute of Uranium Geology, Beijing, China, using a Renishaw RM-2000 Raman microscope. This instrument records peaks in the range of 100–4000 cm^{-1} full-band with a resolution of 1–2 cm^{-1}; the laser beam spot size was about 1 μm. The inclusions were analyzed for the most common gases, monoatomic and polyatomic ions and molecules.

Hydrogen and oxygen isotope compositions were analyzed using a MAT-253 stable isotope ratio mass spectrometer at the Beijing Research Institute of Uranium Geology. Oxygen was analyzed using the BrF_5 extraction technique and hydrogen was measured for vapors released from fluid inclusions in quartz and calcite grains (with a weight of approximate 2 g) by thermal decrepitation. Before hydrogen isotope analysis, the sample was heated to between 100° and 200 °C to decrepitate majority secondary fluid inclusions and thereby largely eliminate their contribution to the isotope composition. Carbon and oxygen isotope compositions of calcites were measured using an IRMS (Isoprime) stable isotope ratio mass spectrometer at State Key Laboratory of Geological Processes and Mineral Resources (GPMR), CUGB. Carbon was released as CO_2 by reacting with phosphoric acid at 25 °C. Isotopic ratios are reported in standard δ notation (‰) relative to SMOW for D-O isotopes and PDB for C-O isotopes. The transformation between SMOW and PDB references for O isotopes is $\delta^{18}O_{SMOW} = 1.03086\delta^{18}O_{PDB} + 30.86$. Analytical precision was better than ± 0.2‰ for $\delta^{18}O$, ± 2‰ for δD, and ± 0.2‰ for $\delta^{13}C$.

The noble gas (He, Ar) isotope analyses were completed by a MI-1201IG inert gas mass spectrometer at the Institute of Mineral Resources, Chinese Academy of Geological Sciences (CAGS). Analytical methods are similar to Kendrick and Burnard (2013). Approximately 200–1000 mg of 0.5–1.0 mm grains were loaded into *vacuo* crushers and baked on-line at < 150 °C for > 24 h to remove absorbed atmospheric gases before crushing. Gases were released from the grains into the all metal extraction system by sequential crushing in modified Nupro type valves. The released gases were exposed to a titanium sponge furnace at 800 °C for 20 min to remove the bulk of active gases

Table 1
Microthermometric fluid inclusion data for different stage veins in the Bianjiadayuan deposit.

Samples	Elevation (m)	Descriptions	Ore stage	N	Th (°C)	Salinity (wt% NaCl equiv)
BJ-01	693	Apy-bearing Qtz vein	I	3	321–350	6.3–11.1
B12-30	730	Apy/Py-bearing Qtz vein	I	2	287–332	5.8–7.3
BJ-12-10	680	Qtz vein in slate	I	2	292–335	4.3–7.2
BJ12-78	592	Sulfide-bearing Qtz vein	II	2	288–313	2.3–4.6
BJ-21	775	Pb-Zn mineralized Qtz vein	II	2	275–302	4.2–6.5
BJ12-24	775	Pb-Zn mineralized Qtz vein	II	1	260–282	4.3–6.2
BJ-35	655	Sulfide-bearing Qtz vein	II	3	265–293	2.1–3.9
BJ12-44	735	Silver-bearing Qtz vein	III	3	230–262	2.5–8.2
BJ12-81	606	Silver-bearing Qtz vein	III	2	210–235	4.6–10.3
BJ12-25	775	Qtz vein in slate	III	1	225–255	0.2–2.2
BJ-12-11	735	Qtz vein in slate	III	1	201–236	2.2–4.3
BJ-06	695	Cal vein in slate	IV	3	163–210	0.3–3.8
BJ12-26	775	Cal vein and veinlet	IV	2	130–162	0.9–3.5
BJ-49	735	Calcite vein in slate	IV	2	120–152	0.2–1.8
BJ-11	695	Cal vein and veinlet	IV	1	145–165	2.1–3.9
BJ-41	775	Cal vein in slate	IV	2	143–172	0.2–1.9

Abbreviation: Th = homogenization temperature, N = the number of analyzed fluid inclusion assemblages (FIA), Apy = arsenopyrite, Py = pyrite, Cal = calcite, Qtz = quartz.

(i.e., H_2O and CO_2), and then exposed to two SAES Zr-Al getters (one at room temperature, the other at 450 °C) for 10 min for further purification. Helium was separated from argon using an activated charcoal cold finger at liquid N_2 temperature (−196 °C) for 40–60 min to trap argon. Gas abundances were measured by peak-height comparison with known amounts of standard air from an air bottle. Procedural blanks were $< 2 \times 10^{-10}$ cm^3 STP ^{4}He and (2–4) $\times 10^{-10}$ cm^3 STP ^{40}Ar, and constituted < 1% of analyzed samples. The blanks were too low to affect calibration of the abundance measurements.

6. Results

6.1. Quartz textures

Scanning electron microscope-cathodoluminescence (SEM-CL) has been used to reveal hydrothermal quartz textures of the studied deposit. Quartz veins from ore stages II and III at Bianjiadayuan typically show oscillatory euhedral growth zones (Fig. 5a and b), and many growth textures are complex and commonly show signs of late healed fractures (Fig. 5a–c). Several quartz samples in stage III associated with Ag mineralization display very fine growth zones (Fig. 5c). Some quartz crystals with euhedral growth zones can be cut by late relatively homogenous quartz crystals (Fig. 5d), reflecting different sequences of quartz precipitation from the ore fluid.

6.2. Fluid inclusions

Fluid inclusions were analyzed microthermometrically in quartz and calcite from different ore stages (I–IV). Only fluid inclusions deemed to be primary from their occurrence in individual grains (Fig. 6a) or along growth zones (Fig. 6b) were selected for the microthermometric studies, and each cluster or set of inclusions along a growth zone was considered to represent a separate fluid inclusion assemblage (FIA). The inclusions in the clusters and along growth zones are elliptical, rod-shaped, rounded, irregular or display negative crystal shapes, and range in length from 10 to 20 μm (Fig. 6). Fluid inclusions occurring along fractures or grain boundaries in clusters and linear arrays were considered secondary and were not analyzed microthermometrically due to their possible late formation.

Fluid inclusions were classified on the basis of the phase relationships observed at room temperature (Fig. 6). Three types of fluid inclusions were identified: (i) liquid-vapor inclusions (L-V, Fig. 6b, g, h), which homogenize to liquid upon heating (they generally contain ~60–80 vol% liquid); (ii) vapor-rich inclusions (V-L, Fig. 6a, e), which homogenize to vapor (they typically contain > 60 vol% vapor); and (iii) monophase vapor or liquid aqueous inclusions (type V or L, Fig. 6c, f). No CO_2-rich fluid inclusions or clathrates were observed. All inclusions types except the monophase inclusions are frequently observed in the examined quartz and calcite samples (Fig. 6a, d), though their relative proportions differ. Significantly, V-L and L-V type inclusions commonly coexist along the same growth zone, providing evidence that the ore fluid underwent phase separation (Fig. 6b, d).

Microthermometric measurements were mainly performed on L-V and V-L type inclusions. Liquid-vapor homogenization and final ice melting temperatures were determined for 32 FIAs from 224 fluid inclusions representing different ore stages (Fig. 7, Table 1). Microthermometric analyses reveal that the homogenization temperatures of FIAs in ore stages I to IV mainly range from 290° to 330 °C, 280° to 310 °C, 220° to 260 °C, and 130° to 190 °C, respectively (Fig. 7). Fluid inclusion assemblages from different ore stages show average liquid-vapor homogenization temperatures of 315 °C, 292 °C, 242 °C and 161 °C, respectively. Variations in salinity, calculated from the final ice melting temperature (T_m) utilizing the equations of Brown (1989), were documented for the four mineralized stages (Fig. 7, Table 1), i.e., from stages I to IV, fluid salinities range from 4.3 to 11.1 (mostly are 4–7 and average in 6.4), 2.1 to 6.5 (mostly are 2–4 and average in 3.7), 0.2 to 10.3 (mostly are 0–8 and average in 4.4), and 0.2 to 3.9 (mostly are 0–2 and average in 1.8) wt% NaCl equiv, respectively.

Laser Raman analyses of individual fluid inclusions indicate that the vapor phase mainly consists of CH_4 and CO_2 (Fig. 8). Generally, fluids in early stages are dominated by CH_4 (Fig. 8a, b), whereas in subsequent late stages fluids are dominated by CH_4 and CO_2 (Fig. 8c, d), demonstrating that CO_2 is common in late stage fluids. However, no CO_2-rich fluid inclusions were observed, although Raman analyses showed that CO_2 is present in the vapor.

6.3. Hydrogen and oxygen isotopes

Hydrogen and oxygen isotope compositions were obtained from vein quartz and calcite in textural equilibrium with stages I to IV sulfides and sulfosalts. Since the hydrogen was not obtained from the OH site in hydrous minerals, the risk of misinterpreting the origin of the mineralizing fluid from the corresponding isotopic ratio was relatively high. The analyzed δD_{H2O} values display a narrow range, i.e., from −139 to −106‰; whereas the measured $\delta^{18}O_{mineral}$ values display a relatively large range, i.e., from −1.1 to +16.3‰ (Table 2). The calculated $\delta^{18}O_{H2O}$ values for the ore fluid in equilibrium with quartz and calcite from stages I to IV, utilizing the equations of quartz- and calcite-water from Zheng (1993) and O'Neil et al. (1969), demonstrate an overall decreasing trend during the hydrothermal fluid evolution, i.e.,

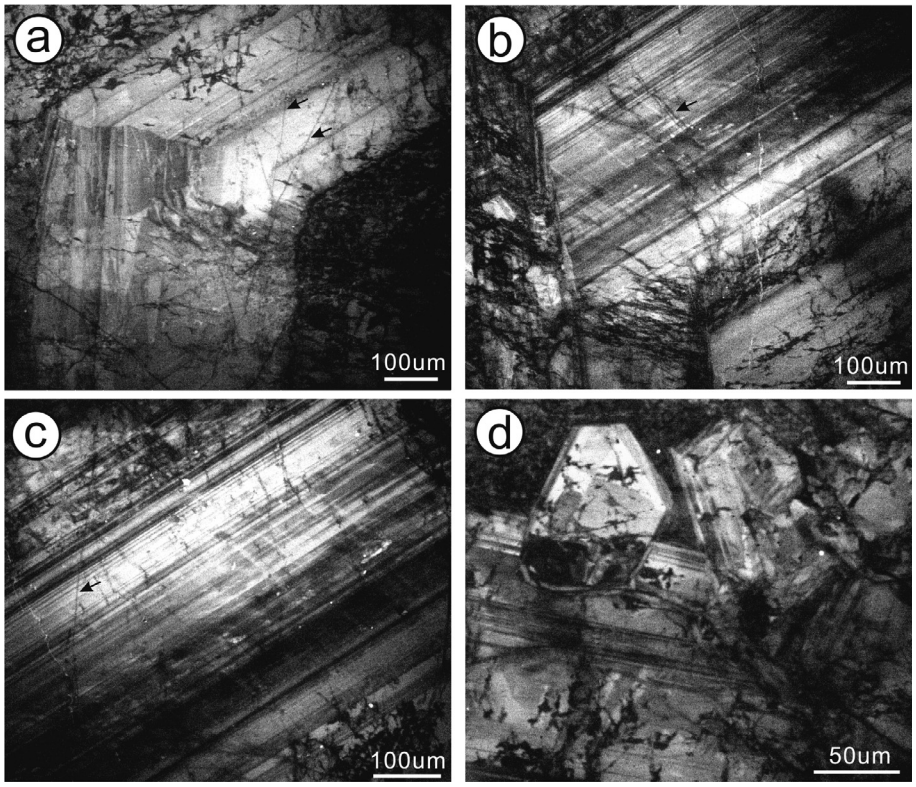

Fig. 5. SEM-CL textures observed in the Bianjiadayuan hydrothermal quartz. (a) Obvious oscillatory euhedral growth zones observed in stage II hydrothermal vein quartz associated with sulfide deposition, cut by CL-dark fractures (arrows indicated); (b)-(c) Oscillatory euhedral fine growth zones observed in stage III hydrothermal vein quartz associated with Ag-sulfosalt deposition, cut by CL-dark fractures (arrows indicated); (d) Quartz with euhedral growth zones cut by late relatively homogenous quartz.

10.7–12.1‰ for stage I, 4.0–7.7‰ for stage II, −3.3 to 1.4‰ for stage III, and −16.4 to −9.2‰ for stage IV (Fig. 9).

6.4. Carbon and oxygen isotopes

A number of 15 calcite samples associated with stage IV boulangerite and illite were collected for measuring their C-O isotopes (Table 3). The analyzed $\delta^{18}O_{SMOW}$ and $\delta^{13}C_{PDB}$ values for calcite samples range from −0.4 to 6.4‰ and −7.7 to −2.7‰, respectively (Table 3).

6.5. Helium and argon isotopes

Noble gas abundance and isotopic data are listed in Table 4. The analytical results show that ^{40}Ar and ^{4}He concentrations range from 10.39 to 42.46 E^{-8} cm^3 STP g^{-1} and 3.94 to 121.28 E^{-8} cm^3 STP g^{-1}, respectively. Measured $^{40}Ar/^{36}Ar$ ratios range from 310.7 to 520.4. The $^{36}Ar/^{38}Ar$ ratios of fluid inclusions in all analyzed samples are relatively uniform and show a narrow range of 5.25–5.37 with an average of 5.31. The $^{3}He/^{4}He$ ratios of fluid inclusions hosted in sulfides are mainly from 1.52 to 3.06 Ra with an average of 2.47 Ra, where Ra represents the $^{3}He/^{4}He$ ratios of the atmosphere with a value of 1.4×10^{-6} (Mamyrin and Tolstikhin, 1984).

7. Discussions

7.1. Temperature-pressure conditions

Homogenization temperatures derived from microthermometric measurements of fluid inclusions provide only a minimum estimate of temperature at the time of fluid trapping. These temperatures represent actual fluid trapping conditions for two-phase fluids in boiling system. The coexistence of vapor-rich and liquid-rich fluid inclusions in one growth zone is evidently suggestive of phase separation during ore formation. Thus, the obtained microthermometric results enable to represent the actual fluid trapping conditions. Fluid inclusion microthermometric results at Bianjiadayuan demonstrate that fluid temperatures for stage II sulfides deposition range from 280° to 310 °C (average 292 °C) and those for stage III Ag-bearing sulfosalts formation range from 220° to 260 °C (average 242 °C) (Fig. 7). Furthermore, fluid inclusion data for stage III Ag-bearing sulfosalt formation are comparable with freibergite crystallization temperatures (i.e., < 250 °C) on the basis of its mineral compositions (Zhai et al., 2018b).

To constrain the pressure conditions of ore deposition in different mineralizing stages, the 'HOKIE FLINCS_H2O-NACL' spreadsheet was used to calculate fluid pressure (Steele-MacInnis et al., 2012). This program can be used to determine properties of fluid inclusions that homogenize to the liquid phase for the H_2O-NaCl system and is generally valid from 21.2° to 700 °C, the LV curve to 6000 bar and 0 to 70 wt% NaCl eqiv. The calculated results for stage I veins show the highest hydrostatic pressures, typically ranging from 70 to 150 bars (average 126 bars). In contrast, the constrained pressures for stage II sulfide and stage III Ag-bearing sulfosalt formation mainly range from 50 to 100 bars (average 78 bars) and 20 to 60 bars (average 36 bars), respectively. Finally, further cooling of hydrothermal fluids to temperatures between 130° and 190 °C for the formation of late boulangerite-calcite veins was accompanied by hydrostatic pressures normally below 30 bars.

Based on fluid inclusion microthermometric results and relevant calculations, we infer that stage II sulfide and stage III Ag-bearing sulfosalt deposition at the Bianjiadayuan deposit predominantly occurred at temperatures of 280° to 310 °C and 220° to 260 °C, and hydrostatic pressures of 50–100 bars and 20 to 60 bars, respectively.

7.2. Constraints on fluid source

Calculated oxygen isotope compositions of hydrothermal fluids in equilibrium with quartz and calcite veins at Bianjiadayuan reveal that stage I has $\delta^{18}O_{H2O}$ values ranging from 10.7 to 12.1‰, stage II from 4.0 to 7.7‰, stage II from −3.3 to 1.4‰, and stage IV from −16.4 to −9.8‰ (Table 2), respectively. The early stage ore fluids (I and II) are characterized by $\delta^{18}O_{H2O}$ values analogous to felsic magmas, though

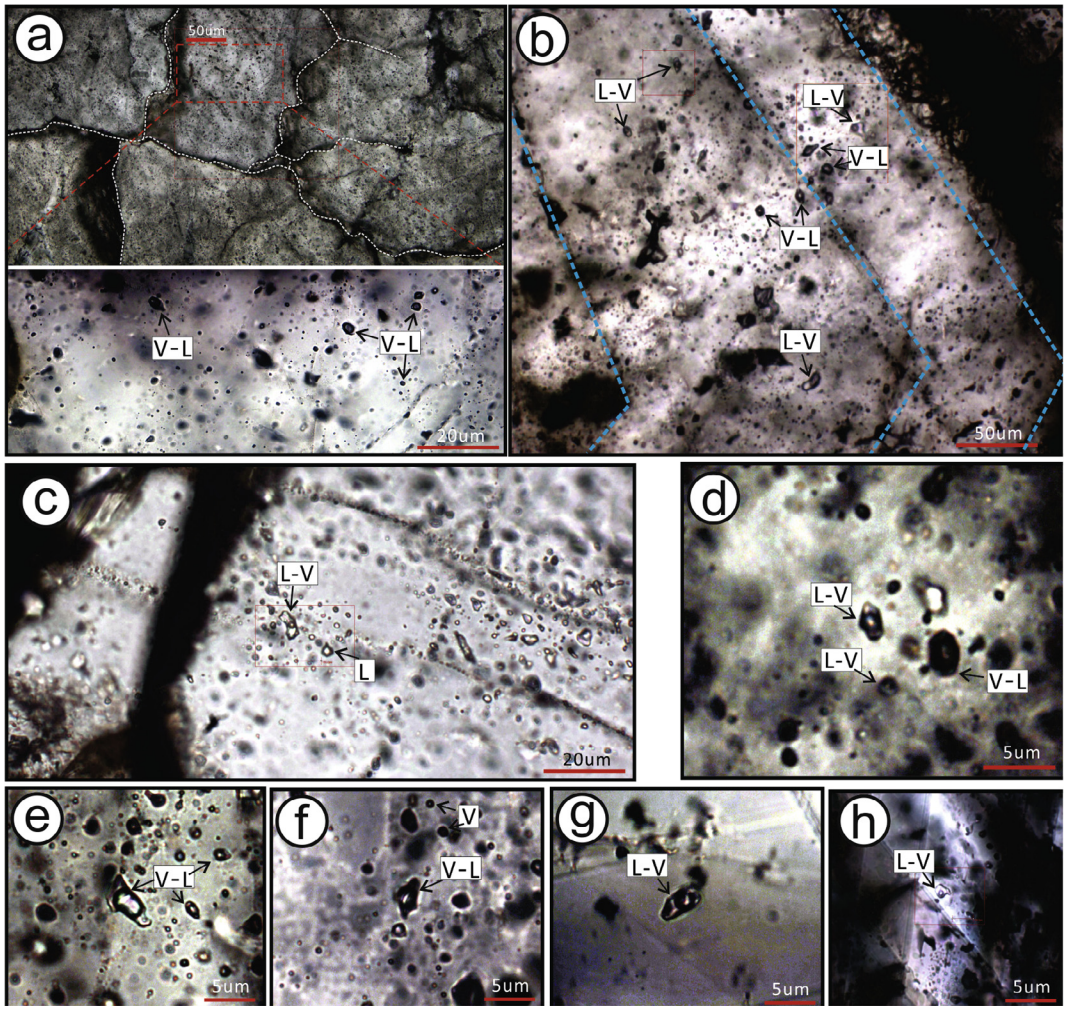

Fig. 6. Photomicrographs of fluid inclusions in quartz and calcite veins at Bianjiadayuan. (a) Different quartz grains and their host primary V-L type inclusions from stage I quartz veins; (b) Fluid inclusion assemblages of L-V and V-L types in different growth zones from stage III quartz veins; (c) The primary inclusions with numerous secondary inclusions in parallel trails aligned along fractures in stage II quartz veins; (d) Fluid inclusion assemblages of L-V and V-L types with variable vapor–liquid ratios from stage III quartz veins; (e) Primary two-phase V-L inclusions (V/L + V = 60–80 vol%) from stage II quartz veins; (f) Primary V-L and V type inclusions from stage III quartz veins; (g)–(h) Primary L-V type inclusions hosted in stage IV calcite veins.

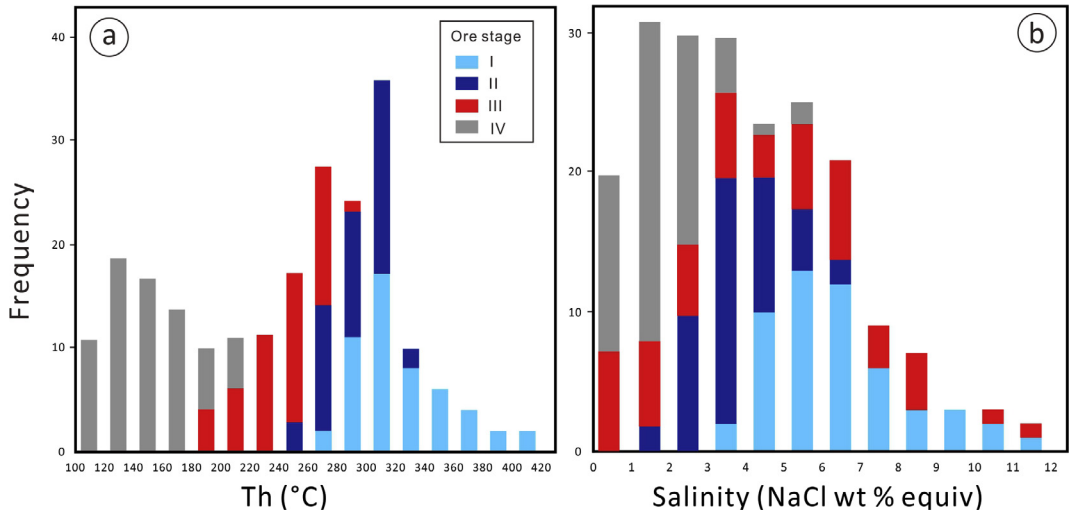

Fig. 7. Homogenization temperature (a) and salinity (b) histograms for fluid inclusions from different stage veins.

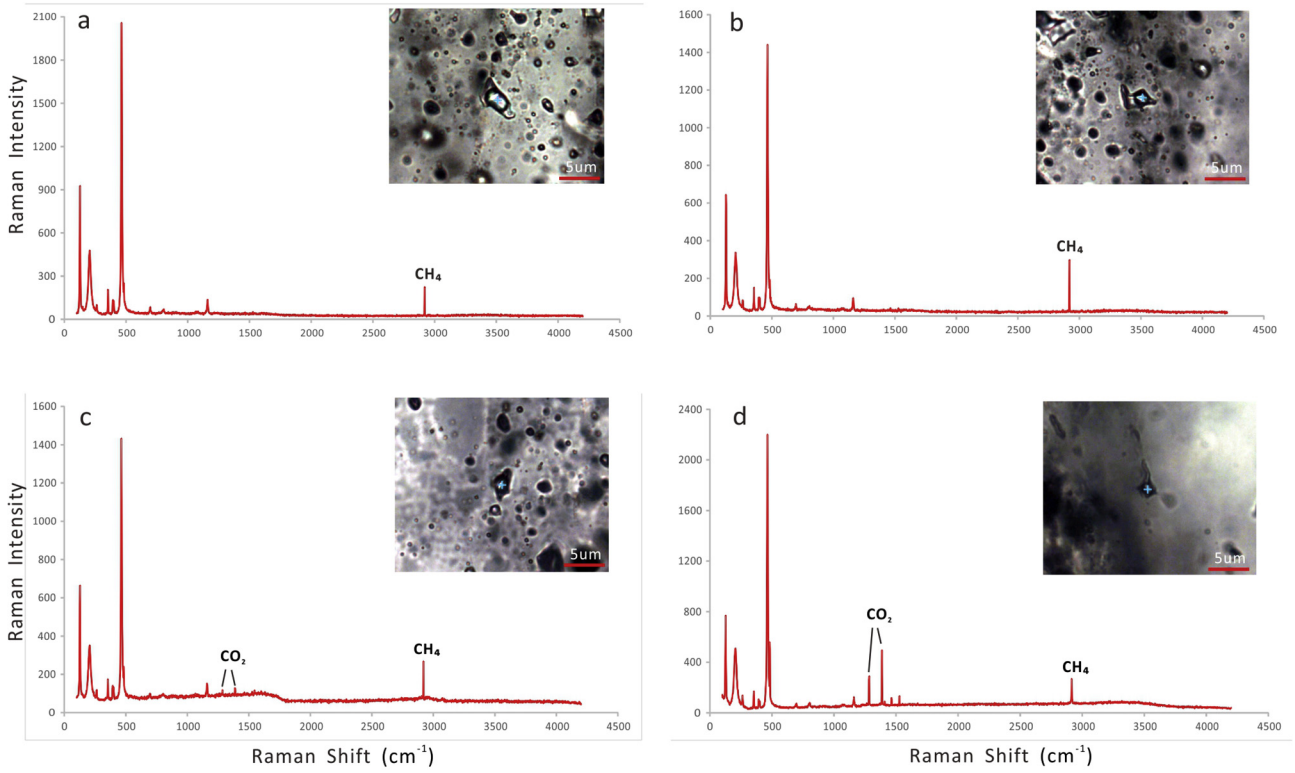

Fig. 8. Laser Raman spectra for fluid inclusions from the Bianjiadayuan deposit. (a)-(b) CH_4-bearing vapor phase inclusions from stage II quartz veins; (c) CO_2- and CH_4-bearing vapor phase inclusions from stage III quartz veins; (d) CO_2- and CH_4-bearing vapor phase inclusions from stage IV calcite veins.

their δD_{H2O} values display a relatively low range (Fig. 10). The obtained δD_{H2O} values suggest mixing and the involvement of meteoric water into the ore fluid, which could lead to the lower δD_{H2O} values. Alternatively, despite our attempt to remove secondary inclusions by heat treating the samples prior to extracting the fluids for isotopic analysis, a variable proportion of secondary inclusions probably failed to decrepitate and these contributed isotopically light meteoric water thereby lowering the δD_{H2O} value of the fluid that was extracted.

There is a distinguished decrease in $\delta^{18}O_{H2O}$ values with temperature decreasing during hydrothermal evolution at Bianjiadayuan (Fig. 9). This is mostly related to a mixing with a meteoric fluid, which is able to result in shifts towards more negative $\delta^{18}O_{H2O}$ values, as the local meteoric waters have much lower $\delta^{18}O$ values relative to the ore fluids. A large completion of D-O isotope data for magmatic-hydrothermal deposits nearby the Bianjiadayuan deposit in the southern GHR has been used for comparisons (Fig. 10). The data suggest that ore fluids responsible for the Bianjiadayuan mineralization are characterized by the addition of greater proportion of meteoric waters in late stages when compared to other ore deposits in the region. The implications from D-O isotopes are consistent with C-O isotopes. The obtained $\delta^{18}O_{SMOW}$ and $\delta^{13}C_{PDB}$ values for waning stage calcites in the studied deposit reveal that their isotopic compositions are very close to an igneous source (Fig. 11a), and distinct from those for marine and sedimentary sources (Fig. 11b), indicating that the studied carbonates are genetically related to a magmatic-hydrothermal fluid. During fluid evolution and cooling, the variations of carbon and oxygen isotope compositions are most probably affected by meteoric water interaction and mixing (Fig. 11b).

Thus, based on the D-O-C isotope compositions, a progressively less magmatic component and increasing meteoric component are responsible for late stage mineral deposition. Accordingly, it is proposed that the early stage ore fluids were typically dominated by magmatic

Table 2
Hydrogen and oxygen isotope compositions of the ore fluids for the Bianjiadayuan deposit (‰).

Samples	Host minerals	Ore stage	Temperature (°C)	$\delta D_{H2O\text{-}SMOW}$	$\delta^{18}O_{mineral\text{-}SMOW}$	$\delta^{18}O_{H2O\text{-}SMOW}$
BJ-01	quartz	I	405	−112	15.1	10.7
BJ12-30	quartz	I	393	−128	16.3	12.1
BJ-21-1	quartz	II	311	−122	9.8	4.0
BJ12-24	quartz	II	310	−109	13.5	7.7
BJ12-44	quartz	III	249	−129	4.3	−3.3
BJ12-81	quartz	III	223	−121	10.0	1.4
BJ-06	calcite	IV	148	−132	2.5	−9.8
BJ-11	calcite	IV	152	−139	0.4	−14.9
BJ-49	calcite	IV	159	−121	1.6	−13.1
BJ-21-2	calcite	IV	152	−126	−1.1	−16.4
BJ-36	calcite	IV	152	−133	0.7	−14.6
BJ-12-25	calcite	IV	157	−106	0.8	−14.1
BJ-12-39	calcite	IV	152	−123	−0.4	−15.7

Note: The $\delta^{18}O_{H2O}$ values are calculated based on quartz-water and calcite-water oxygen isotope fractionation equations of Zheng (1993) and O'Neil et al. (1969), respectively; temperature used in the calculations are derived from fluid inclusion microthermometric data.

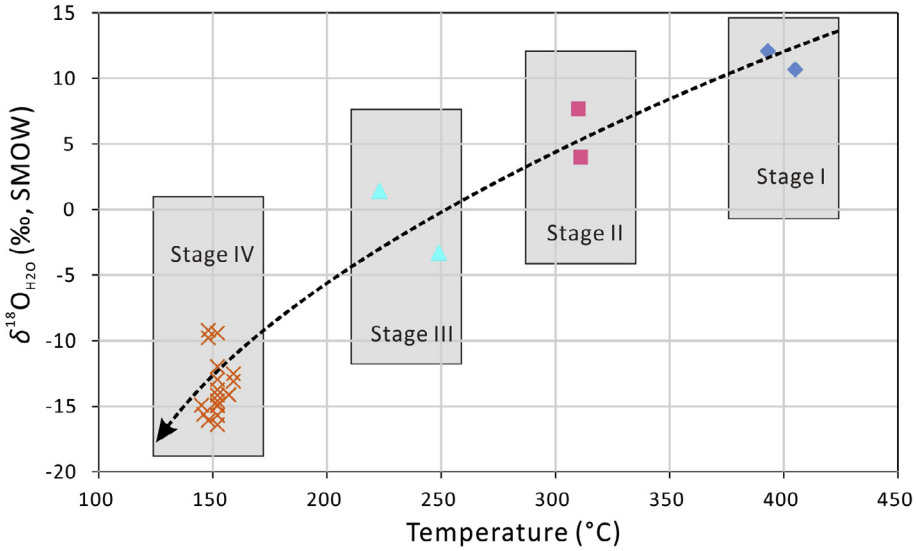

Fig. 9. $\delta^{18}O_{H2O}$ versus temperature plots for the Bianjiadayuan mineralizing fluids.

Table 3
Carbon and oxygen isotope compositions of calcites for the Bianjiadayuan deposit (‰).

Samples	$\delta^{13}C_{PDB}$	$\delta^{18}O_{PDB}$	$\delta^{18}O_{SMOW}$
BJ-07	−2.7	−23.7	6.4
BJ-12	−4.8	−29.0	1.0
BJ-50	−4.0	−27.8	2.2
BJ-41	−4.0	−30.3	-0.4
BJ-37	−3.8	−27.7	2.3
BJ12-04	−5.8	−28.4	1.6
BJ12-14	−6.1	−29.7	0.2
BJ12-19	−5.1	−28.8	1.1
BJ12-26	−5.6	−29.2	0.7
BJ12-30	−6.5	−26.7	3.3
BJ12-37	−6.9	−30.3	−0.4
BJ12-82	−7.7	−24.2	5.9
BJ12-88	−5.8	−29.6	0.3

fluid, whereas the late stage ore fluids contained a significant proportion of meteoric water.

The $^3He/^4He$ ratios of fluid inclusions extracted from sulfides exhibit higher values (1.52–3.06 Ra) relative to those of continental crust-derived He (i.e., 0.01–0.05 Ra, Stuart et al., 1995). Although the obtained $^3He/^4He$ ratios of ore minerals in the deposit are not as high as the subcontinental lithospheric mantle value (i.e., 6–7 Ra, Burnard et al., 1999), their ratios clearly demonstrate a contribution of mantle-derived fluid (i.e., magmatic fluid) in the Bianjiadayuan ore system. In the $^3He/^4He$ versus $^{40}Ar/^{36}Ar$ (Fig. 12a) and $^{40}Ar^*/^4He$ (Fig. 12b) plots, the noble gas isotopic data confirm a significant contribution of mantle helium into the Bianjiadayuan hydrothermal system. This identification is consistent with the origin of ore fluids for several base metal vein type ore deposits in the southern GHR (Fig. 12).

During the Early Cretaceous when several ore deposits formed in NE China, the most significant tectonic process involved the subduction of the Paleo-Pacific plate beneath the Eurasian plate and its subsequent roll-back with regional lithospheric delamination (Zhang et al., 2010; Wu et al., 2011). In such a tectonic setting, due to the addition of the radiogenic helium from the lower/upper crustal materials, a mantle fluid source would show helium isotopic ratios lower than the typical MORB (i.e., 8 Ra; Ozima and Podosek, 2002). Hence, an initial $^3He/^4He$ ratio of 6 Ra is assumed to be similar to the subcontinental lithospheric mantle value for an enriched mantle fluid in NE China during the Late Mesozoic (Zhai et al., 2015). Based on the equation of Anderson (2000), the calculated He isotope values for the Bianjiadayuan deposit suggest a range from 25 to 51% of mantle-sourced helium (Table 4). Consequently, the He and Ar isotopic compositions reveal that the ore-forming fluids responsible for main sulfide ore formation are dominantly derived from a magmatic fluid with minor crustal fluid addition.

7.3. Fluid evolution

Fluid inclusion microthermometric results reveal a continuous cooling of the ore fluid through time, as determined from decreasing average temperatures from early to late ore stages. A trend of temperature decrease with fluid salinity decrease is obvious from the Th versus salinity plots (Fig. 13), indicating the occurrence of a fluid mixing. The early fluid with characteristics of relatively high temperature (i.e., 290–330 °C) and salinity is mostly related to the origin of the ore-forming fluids from a felsic magma, as evidenced from the noble gas isotope compositions of ore minerals. This is also consistent with sulfur and lead isotope compositions of sulfides, which indicate the origin of S, Pb and other metals from a felsic magma (Zhai et al.,

Table 4
Noble gas compositions (E^{-8} cm^3 STP g^{-1}) and isotopic ratios of fluid inclusions trapped in sulfides from the Bianjiadayuan deposit.

Samples	Minerals	^{40}Ar	^4He	$^{40}Ar/^{36}Ar$	$^{36}Ar/^{38}Ar$	$^3He/^4He$ (1 0 $^{-7}$)	$^3He/^4He$ (Ra)	$^{40}Ar^*$	$^4He_{mantle}$ (wt %)
BJ-12-27	Sphalerite	17.64	15.51	314.0 ± 0.2	5.28 ± 0.01	35.31 ± 0.63	2.52	1.04	41.9
BJ12-86-3	Pyrite	13.81	17.18	317.6 ± 0.3	5.37 ± 0.01	21.32 ± 0.88	1.52	0.96	25.3
BJ-1	Sphalerite	42.46	121.28	520.4 ± 0.6	5.32 ± 0.01	42.86 ± 0.97	3.06	18.35	50.9
BJ-2-2	Galena	10.39	3.94	310.7 ± 0.3	5.25 ± 0.01	38.75 ± 2.44	2.77	0.51	46.0

Note: Ra is the $^3He/^4He$ ratios of the atmosphere (1.4×10^{-6}, Mamyrin and Tolstikhin, 1984); $^{40}Ar^*$ is non-atmospheric ^{40}Ar, which can be expressed as $^{40}Ar^* = {}^{40}Ar_{sample} - 295.5 \times {}^{36}Ar_{sample}$; $^4He_{mantle}$ values represent weight percent of mantle helium compared with crustal helium, which could be calculated as $^4He_{mantle}$ (wt %) = $100[(^3He/^4He)_{sample} - (^3He/^4He)_{crust}]/[(^3He/^4He)_{mantle} - (^3He/^4He)_{crust}]$, assuming a mantle R/Ra = 6.00 and crustal R/Ra = 0.01 (Anderson, 2000).

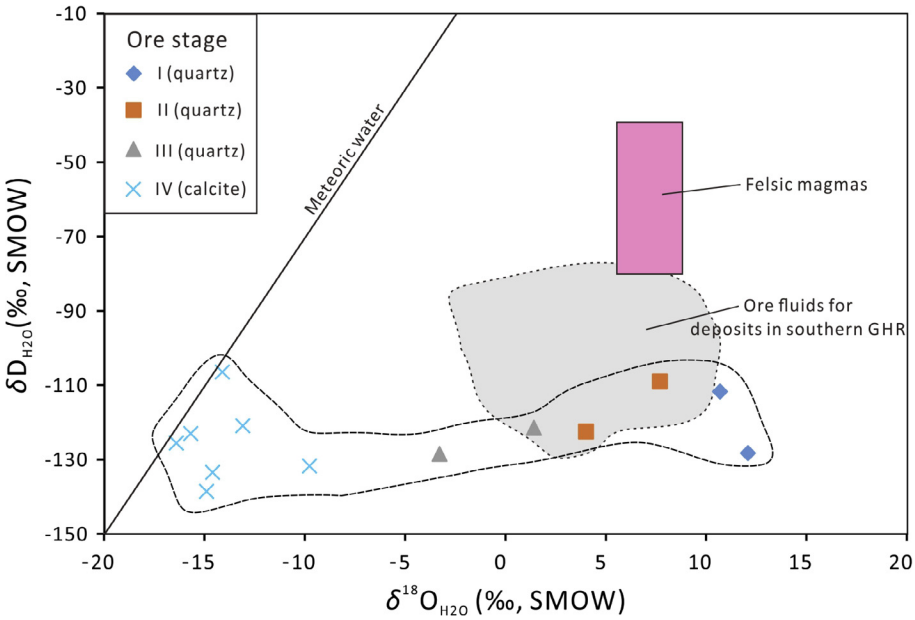

Fig. 10. $\delta^{18}O$ versus δD isotope compositions of the Bianjiadayuan mineralizing fluids. The field of felsic magma and meteoric water line are from Hedenquist and Lowenstern (1994) and Hoefs (2009), respectively. The field representing of the D-O isotope compositions of ore fluids for deposits in the GHR is from Ouyang et al. (2015).

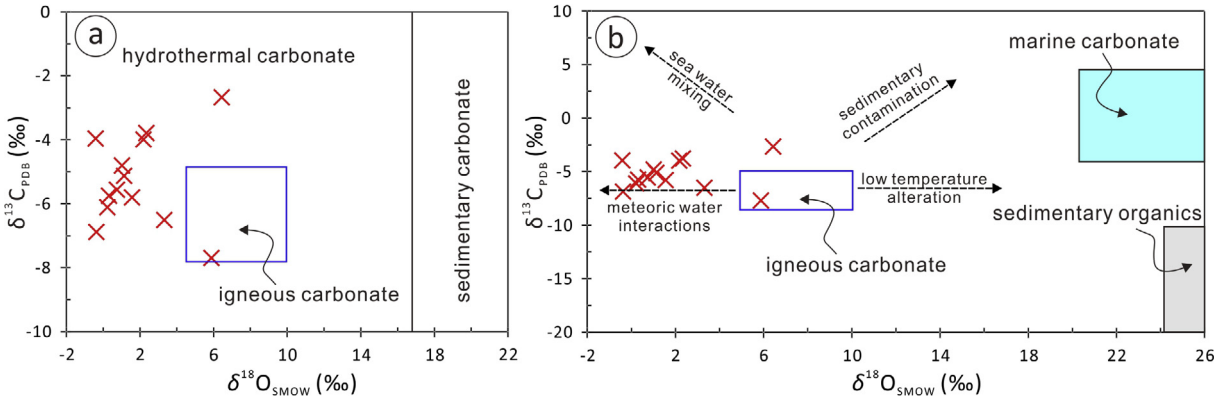

Fig. 11. $\delta^{18}O$ versus $\delta^{13}C$ isotope compositions of late stage calcites in the Bianjiadayuan deposit. (a) Genetic type for calcite formation (based on Liu et al., 2016b); (b) Geological events responsible for carbon and oxygen isotope variations (based on Demény et al., 1998; Liu et al., 2004).

2018b). By contrast, the waning stage fluid with characteristics of relatively low temperature (i.e., 130–190 °C) and salinity (i.e., 0.2–2.0 wt % NaCl equiv) is closely associated with addition of large volumes of meteoric waters, consistent with D-O and C-O isotope signatures for late stage carbonates (Figs. 10 and 11b). For stage III where abundant Ag-bearing minerals formed, the fluid was marked with an increase in salinity (i.e., from 0.2 to 10.3 wt% NaCl equiv) with drop in temperature (Fig. 13), which is suggestive of phase separation, i.e., fluid boiling. Evidence for fluid phase separation is also provided by the coexistence of liquid-rich and vapor-rich fluid inclusions in one growth zone (Fig. 6b, d). At relatively shallow levels, the meteoric waters can easily mix into the hydrothermal system as boiling of the ore fluid assists the conduits to open, and increases permeability of host rocks.

In summary, fluid inclusion microthermometry indicates that vein formation at the Bianjiadayuan hydrothermal system occurred at progressively lower temperature and pressure. Hydrothermal fluid cooling, phase separation, and mixing with meteoric waters are advocated as the important causes for ore deposition.

7.4. Genetic model and exploration implications

A genetic model of a magmatic-hydrothermal origin is proposed for formation of Ag-Pb-Zn veins at Bianjiadayuan district (Fig. 14), which is supported by the following collective lines of evidences. Field investigation identified that the Ag-Pb-Zn veins occurred adjacent to a Sn ± Cu ± Mo mineralized porphyry intrusion within several hundred meters (Fig. 2a), demonstrating a close spatial association between those two mineralization types. Furthermore, clear alteration (i.e., from porphyry center outwards showing potassic, phyllic and propylitic alteration) and metal zonation (i.e., Sn ± Cu ± Mo, Sn-Zn to Ag-Pb-Zn; Wang et al., 2014) that have been identified in the ore district reveal a porphyry ore system. Sulfur and lead isotope compositions indicate the origin of sulfur, lead and other metals from a magma (Zhai et al., 2018b), which is consistent with the noble gas isotopes displaying evidence of a magmatic fluid responsible for the vein type ore formation (i.e., R/Ra values of 1.52–3.06) (Fig. 12). The present studies of D-O-C isotopes and fluid inclusion indicate that the early stage ore fluids were typically dominated by a magmatic fluid, whereas fluids for late stage contained a significant proportion of meteoric waters (Figs. 10 and 11b). Geochronological studies reveal that the porphyry mineralization with molybdenite Re-Os ages of 140.0 ± 1.7 Ma is indistinguishable within error from Ag-Pb-Zn vein mineralization with a sericite $^{40}Ar/^{39}Ar$ age of 138.7 ± 1.0 Ma (Zhai et al., 2017). Both local porphyry type and vein type mineralization occurred at Bianjiadayuan district is attributed to the fluids released from the porphyry magma. This has also been suggested for the formation of some ore deposits in the GHR (i.e., the Weilasituo ore district with porphyry Sn and Cu-Zn-Ag vein type mineralization, Wang et al., 2017) as well as other region

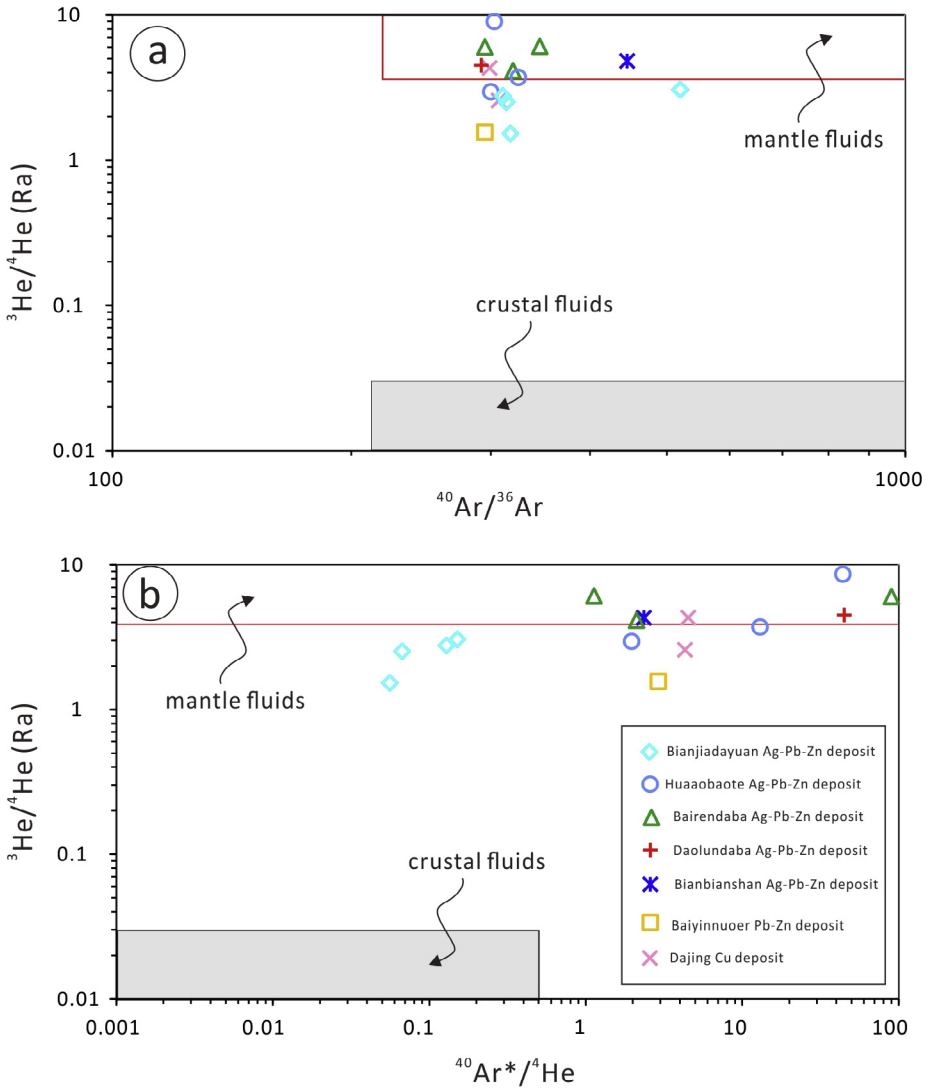

Fig. 12. $^{40}Ar/^{36}Ar$ versus $^{3}He/^{4}He$ (a) and $^{40}Ar^{*}/^{4}He$ versus $^{3}He/^{4}He$ (b) plots of different sulfides from numerous ore deposits in the southern GHR district. Helium and argon isotopes from the Bianjiadayuan deposit are from this study, and those for other ore deposits are from Niu et al. (2011). The noble gas fields for crustal and mantle fluids are based on Shen et al. (2013).

(i.e., the Plaka ore district with porphyry and vein type mineralization, Voudouris et al., 2008).

In summary, an integrated evidences of geological, multiple isotope, fluid inclusion and geochronological investigations consistently support a close spatial-temporal-genetic relationship between local Ag-Pb-Zn mineralized veins and Sn ± Cu ± Mo mineralized porphyry intrusion at Bianjiadayuan ore district. Thus, a magmatic-hydrothermal model for Ag-Pb-Zn vein formation at Bianjiadayuan district is established (Fig. 14), indicating that the local porphyry Sn ± Cu ± Mo mineralization and Ag-Pb-Zn veins are genetically related. This model is helpful for ore exploration and targeting in the region. Future ore exploration in the district should target potential Ag-Pb-Zn veins in the western part of the ore distinct, as the current mining of these veins dominantly focus on the eastern part. Exploration targeting should give emphasis to altered areas along with faults (or crosscutting faults), which are highly favorable for such vein type mineralization, spatially close to the porphyry intrusion.

8. Conclusions

The available geological, multiple isotope, geochronological and fluid inclusion investigations of Ag-Pb-Zn mineralized veins at Bianjiadayuan ore district provide compelling evidences that ore-forming fluids were genetically related to a Sn ± Cu ± Mo mineralized porphyry intrusion. Stable (D-O-C) and noble gas isotope compositions consistently indicate the origin of ore-forming fluids from a typical magmatic-hydrothermal fluid. Fluid inclusion studies reveal that the Ag-Pb-Zn vein formation at Bianjiadayuan occurred at progressively lower temperature and pressure. Fluid cooling, phase separation, and mixing with meteoric waters are advocated as the important factors for ore deposition. In combination, the present data for the Bianjiadayuan ore district suggest a genetically related porphyry ore system with proximal porphyry type Sn ± Cu ± Mo mineralization and peripheral Ag-Pb-Zn veins, which is a useful concept for local and regional Ag-Pb-Zn exploration targeting.

Acknowledgements

This research was supported financially by the National Natural Science Foundation of China (Grants 41672068, 41272110), the Fundamental Research Funds for the Central Universities (Grant 2652015045), the Open Research Funds for GPMR (Grant GPMR201513) and the Chinese “111” project (Grant B07011). We thank Aihua Liu for the C-O isotope analyses, Li Chen for the SEM-CL

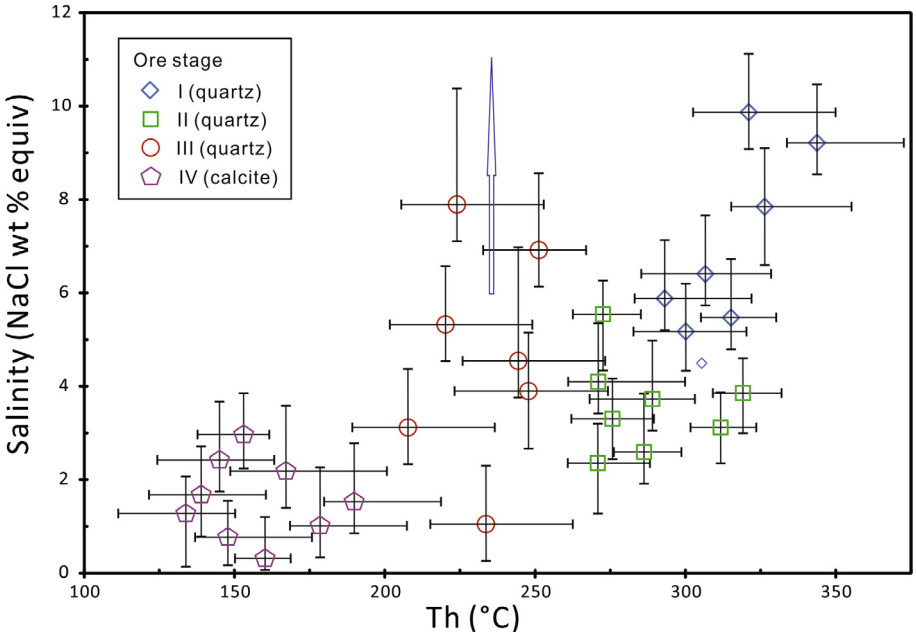

Fig. 13. Homogenization temperature versus salinity plots for fluid inclusions from the Bianjiadayuan deposit. Arrow symbol represents the fluid boiling episode.

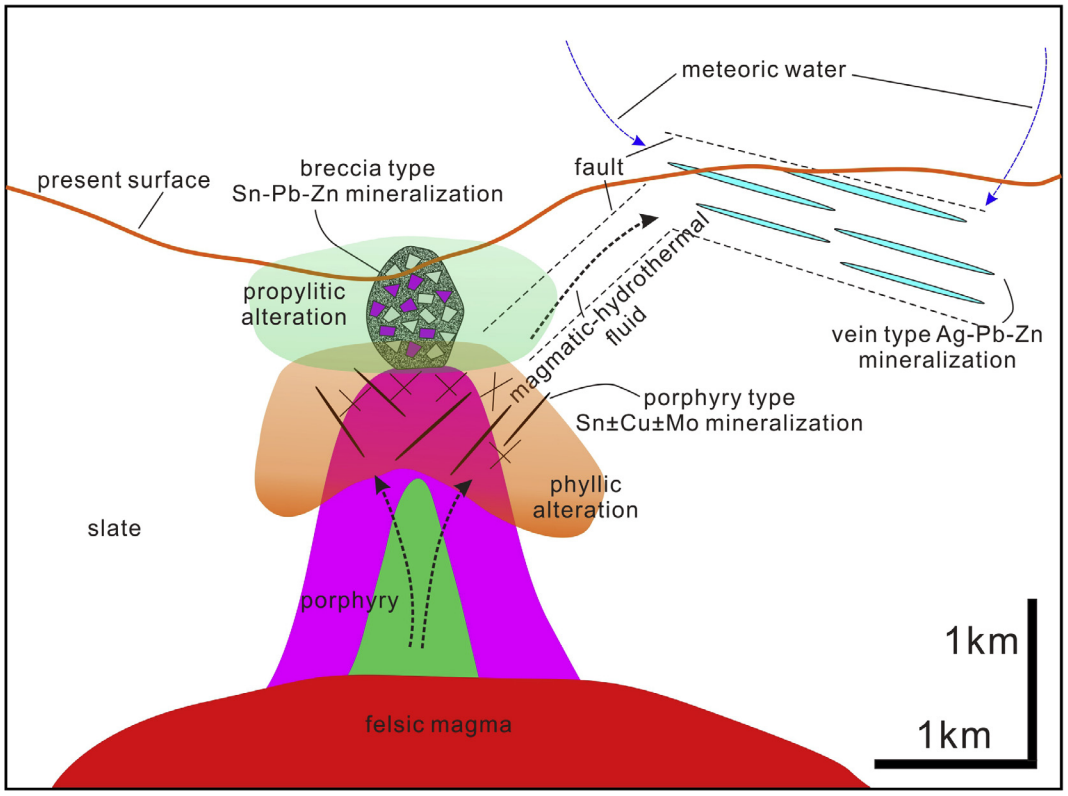

Fig. 14. A proposed genetic model for Ag-Pb-Zn vein formation at Bianjiadayuan ore district.

analyses, and Guangxi Ou for the Raman analyses. Xilong Wang, Qibin Zhang, Kuan Li, Chaoyun Jiang and Peilin Li are thanked for the field help and sample preparation. Lluís Fontboté is thanked for reading the early draft and numerous suggestions. Two anonymous reviewers are thanked for their helpful suggestions that improve this paper, and Editor-in-Chief Dr. Franco Pirajno and Associate Editor Dr. Zhaochong Zhang are thanked for the editorial help.

Appendix A. Supplementary data

Supplementary data associated with this article can be found, in the online version, at https://doi.org/10.1016/j.oregeorev.2018.07.005.

References

Anderson, D.L., 2000. The statistics and distribution of helium in the mantle. Int. Geol. Rev. 42, 289–311.
Brown, P.E., 1989. FLINCOR: a microcomputer program for the reduction and

investigation of fluid inclusion data. Am. Mineral. 74, 1390–1393.
Burnard, P.G., Hu, R.Z., Turner, G., Bi, X.W., 1999. Mantle, crustal and atmospheric noble gases in Ailaoshan gold deposits, Yunnan Province. China. Geochim. Cosmochim. Acta 63, 1595–1604.
Catchpole, H., Kouzmanov, K., Putlitz, B., Seo, J.H., Fontboté, L., 2015. Zoned base metal mineralization in a porphyry system: Origin and evolution of mineralizing fluids in the Morococha district. Peru. Econ. Geol. 110, 39–71.
Chen, B., Jahn, B.M., 2001. Geochemical and isotopic studies of the sedimentary and granitic rocks of the Altai Orogen of NW China and their tectonic implications. Geol. Mag. 139, 1–13.
Chen, Y.J., Chen, H.Y., Zaw, K., Pirajno, F., Zhang, Z.J., 2007. Geodynamic settings and tectonic model of skarn gold deposits in China: an overview. Ore Geol. Rev. 31, 139–169.
Chen, Y.J., Zhang, C., Wang, P., Pirajno, F., Li, N., 2017. The Mo deposits of Northeast China: a powerful indicator of tectonic settings and associated evolutionary trends. Ore Geol. Rev. 81, 602–640.
Demény, A., Ahijado, A., Casillas, R., Vennemann, T.W., 1998. Crustal contamination and fluid/rock interaction in the carbonatites of Fuerteventura (Canary Islands, Spain): a C, O, H isotope study. Lithos 44, 101–115.
Gao, J., Klemd, R., Zhu, M., Wang, X., Li, J., Wan, B., Xiao, W., Zeng, Q., Shen, P., Sun, J., Qin, K., 2017. Large-scale porphyry-type mineralization in the Central Asian metallogenic domain: A review. J. Asian Earth Sci. 1–30. https://doi.org/10.1016/j.jseaes.2017.10.002.
HBGMR (Heilongjiang Bureau of Geology and Mineral Resources),, 1993. Regional Geology of Heilongjiang Province. Geological Publishing House, Beijing, pp. 347–418 (in Chinese with English abstract).
Hedenquist, J.W., Arribas, A.J., Reynolds, T.J., 1998. Evolution of an intrusion-centered hydrothermal system: far Southeast-Lepanto porphyry and epithermal Cu-Au deposits. Philippines. Econ. Geol. 93, 373–404.
Hedenquist, J.W., Lowenstern, J.B., 1994. The role of magmas in the formation of hydrothermal ore deposits. Nature 370, 519–527.
Heinrich, C.A., 2005. The physical and chemical evolution of low-salinity magmatic fluids at the porphyry to epithermal transition: a thermodynamic study. Miner. Deposita 39, 864–889.
Hoefs, J., 2009. Stable Isotope Geochemistry. Springer-Verlag, Berlin.
Jahn, B.M., Wu, F., Chen, B., 2000. Granitoids of the Central Asian Orogenic Belt and continental growth in the Phanerozoic. Trans. R. Soc. Edinburgh: Earth Sci. 91, 181–193.
Kendrick, M.A., Burnard, P., 2013. Noble gases and halogens in fluid inclusions: A journey through the Earth's crust. In: Burnard, P. (Ed.), The Noble Gases as Geochemical Tracers. Springer, Berlin Heidelberg, pp. 319–369.
Kissin, S.A., Mango, H., 2014. Silver Vein Deposits. Treatise on Geochemistry, Second. Edition. Elsevier, Oxford, pp. 425–432.
Li, W.B., Zhong, R.C., Xu, C., Song, B., Qu, W.J., 2012. U-Pb and Re–Os geochronology of the Bainaimiao Cu–Mo–Au deposit, on the northern margin of the North China Craton, Central Asia Orogenic Belt: implications for ore genesis and geodynamic setting. Ore Geol. Rev. 48, 139–150.
Liu, C., Bagas, L., Wang, F., 2016a. Isotopic analysis of the super-large Shuangjianzishan Pb–Zn–Ag deposit in Inner Mongolia, China: Constraints on magmatism, metallogenesis, and tectonic setting. Ore Geol. Rev. 75, 252–267.
Liu, J., He, M., Li, Z., Liu, Y., Li, C., Zhang, Q., Yang, W., Yang, A., 2004. Oxygen and carbon isotopic geochemistry of Baiyangping silver-copper polymetallic ore concentration area in Lanping basin of Yunnan province and its significance. Mineral Deposits 23, 1–10 (in Chinese with English abstract).
Liu, X., Li, W., Xiao, W., Wei, Y., 2016b. Multiple sources and genesis of the Suoerkuduke Cu-Mo deposit during the Carboniferous, East Junggar: insights from zircon U-Pb age and C-O-S-Pb isotopes. Ore Geol. Rev. https://doi.org/10.1016/j.oregeorev.2016.10.031.
Liu, Y., Jiang, S., Bagas, L., 2016c. The genesis of metal zonation in the Weilasituo and Bairendaba Ag–Zn–Pb–Cu–(Sn–W) deposits in the shallow part of a porphyry Sn–W–Rb system, Inner Mongolia. China. Ore Geol. Rev. 75, 150–173.
Mamyrin, B.A., Tolstikhin, I.N., 1984. Helium isotopes in nature. Elsevier, Amsterdam, pp. 1–267.
Mao, J.W., Xie, G.Q., Zhang, Z.H., Li, X.F., Wang, Y.T., Zhang, C.Q., Li, Y.F., 2005. Mesozoic large-scale metallogenic pluses in North China and corresponding geodynamic settings. Acta Petrol. Sin. 21, 169–188 (in Chinese with English abstract).
Melfos, V., Voudouris, P., 2017. Cenozoic metallogeny of Greece and potential for precious, critical and rare metals exploration. Ore Geol. Rev. 89, 1030–1057.
Muntean, J.L., Einaudi, M.T., 2000. Porphyry gold deposits of the Refugio district, Maricunga belt, northern Chile. Econ. Geol. 95, 1445–1472.
Niu, S.Y., Nie, F.J., Sun, A.Q., Jiang, S.H., 2011. Mantle branch structure and silver polymetallic mineralization in the Da Hinggan Mountains, Inner Mongolia. J. Jilin Univ. (Earth Sci. Ed.) 41, 1944–1958 (in Chinese with English abstract).
O'Neil, J.R., Clayton, R.N., Mayeda, T.K., 1969. Oxygen isotope fractionation in divalent metal carbonates. J. Chem. Phys. 51, 5547–5558.
Ouyang, H., Mao, J., Santosh, M., Wu, Y., Hou, L., Wang, X., 2014. The Early Cretaceous Weilasituo Zn–Cu–Ag vein deposit in the southern Great Xing'an Range, northeast China: fluid inclusions, H, O, S, Pb isotope geochemistry and genetic implications. Ore Geol. Rev. 56, 503–515.
Ouyang, H., Mao, J., Zhou, Z., Su, H., 2015. Late Mesozoic metallogeny and intracontinental magmatism, southern Great Xing'an Range, northeastern China. Gondwana Res. 27, 1153–1172.
Ozima, M., Podosek, F.A., 2002. Noble Gas Geochemistry, second ed. Cambridge University Press, Cambridge, pp. 1–286.
Reed, M., Rusk, B., Palandi, J., 2013. The Butte magmatic-hydrothermal system: one fluid yields all alteration and veins. Econ. Geol. 108, 1379–1396.
Rottier, B., Kouzmanov, K., Casanova, V., Bouvier, A.S., Baumgartner, L.P., Wälle, M., Fontboté, L., 2018. Mineralized breccia clasts: a window into hidden porphyry-type mineralization underlying the epithermal polymetallic deposit of Cerro de Pasco (Peru). Miner. Deposita 1–28. https://doi.org/10.1007/s00126-017-0786-9.
Ruan, B., Lv, X., Yang, W., Liu, S., Yu, Y., Wu, C., Adam, M.M.A., 2015. Geology, geochemistry and fluid inclusions of the Bianjiadayuan Pb–Zn–Ag deposit, Inner Mongolia, NE China: implications for tectonic setting and metallogeny. Ore Geol. Rev. 71, 121–137.
Seedorff, E., Dilles, J.H., Proffett, J.M., Einaudi, M.T., Zurcher, L., Stavast, W.J.A., Johnson, D.A., Barton, M.D., 2005. Porphyry deposits: characteristics and origin of hypogene features. Econ. Geol., 100th Anniversary volume, 251–298.
Shen, J.F., Santosh, M., Li, S.R., Zhang, H.F., Yin, N., Dong, G.C., Wang, Y.J., Ma, G.G., Yu, H.J., 2013. The Beiminghe skarn iron deposit, eastern China: geochronology, isotope geochemistry and implications for the destruction of the North China Craton. Lithos 156, 218–229.
Shu, Q., Chang, Z., Lai, Y., Zhou, Y., Sun, Y., Yan, C., 2016. Regional metallogeny of Mo-bearing deposits in northeastern China, with new Re-Os dates of porphyry Mo deposits in the northern Xilamulun district. Econ. Geol. 111, 1783–1798.
Sillitoe, R.H., 2010. Porphyry copper systems. Econ. Geol. 105, 3–41.
Sillitoe, R.H., Mortensen, J.K., 2010. Longevity of porphyry copper formation at Quellaveco. Peru. Econ. Geol. 105, 1157–1162.
Steele-MacInnis, M., Lecumberri-Sanchez, P., Bodnar, R.J., 2012. HOKIEFLINCS_H2O-NACL: A Microsoft Excel spreadsheet for interpreting microthermometric data from fluid inclusions based on the PVTX properties of H_2O-NaCl. Compu. Geosci. 49, 334–337.
Stuart, F.M., Burnard, P.G., Taylor, R.P., Turner, G., 1995. Resolving mantle and crustal contributions to ancient hydrothermal fluids: He-Ar isotopes in fluid inclusions from Dae Hwa W-Mo mineralisation, South Korea. Geochim. Cosmochim. Acta 59, 4663–4673.
Voudouris, P., Melfos, V., Spry, P.G., Bonsall, T., Tarkian, M., Economou-Eliopoulos, M., 2008. Mineralogical and fluid inclusion constraints on the evolution of the Plaka intrusion-related ore system, Lavrion, Greece. Miner. Petrol. 93, 79–110.
Voudouris, P.C., Melfos, V., Spry, P.G., Kartal, T., Schleicher, H., Moritz, R., Ortelli, M., 2013. The Pagoni Rachi/Kirki Cu-Mo ± Re ± Au deposit, northern Greece: mineralogical and fluid inclusion constraints on the evolution of a telescoped porphyry-epithermal system. Can. Mineral. 51, 253–284.
Wang, F., Bagas, L., Jiang, S., Liu, Y., 2017. Geological, geochemical, and geochronological characteristics of Weilasituo Sn-polymetal deposit, Inner Mongolia, China. Ore Geol. Rev. 80, 1206–1229.
Wang, F., Zhou, X.H., Zhang, L.C., Ying, J.F., Zhang, Y.T., Wu, F.Y., 2006. Late Mesozoic volcanism in the Great Xing'an Range (NE China): timing and implications for the dynamic setting of NE Asia. Earth Planet. Sci. Lett. 251, 179–198.
Wang, X., Liu, J., Zhai, D., Yang, Y., Wang, J., Zhang, Q., Zhang, A., Wang, X., 2013. LA-ICP-MS zircon U-Pb dating, geochemistry of the intrusive rocks from the Bianjiadayuan Pb-Zn-Ag deposit, Inner Mongolia, China and tectonic implications. Geotect. Metall. 37, 730–742 (in Chinese with English abstract).
Wang, Y., Cai, T., Bao, N., Li, W., Nie, T., Da, Y., Sun, Y., 2014. Geological characteristic and control factors in Bianjiadayuan Pb-Zn-Ag deposit, Inner Mongolia. J. East China Inst. Tec. (Nat. Sci.) 37, 212–219 (in Chinese with English abstract).
Wei, C.S., Zhao, Z.F., Spicuzza, M.J., 2008. Zircon oxygen isotopic constraint on the sources of late Mesozoic A-type granites in eastern China. Chem. Geol. 250, 1–15.
Wu, F.Y., Jahn, B.M., Wilde, S.A., Lo, C.H., Yui, T.F., Lin, Q., Ge, W.C., Sun, D.Y., 2003. Highly fractionated I-type granites in NE China (I): geochronology and petrogenesis. Lithos 66, 241–273.
Wu, F.Y., Lin, J.Q., Wilde, S.A., Zhang, X.O., Yang, J.H., 2005. Nature and significance of the Early Cretaceous giant igneous event in eastern China. Earth Planet. Sci. Lett. 233, 103–119.
Wu, F.Y., Sun, D.Y., Ge, W.C., Zhang, Y.B., Grant, M.L., Wilde, S.A., Jahn, B.M., 2011. Geochronology of the Phanerozoic granitoids in northeastern China. J. Asian Earth Sci. 41, 1–30.
Wu, F.Y., Wilde, S.A., Sun, D.Y., Zhang, G.L., 2004. Geochronology and petrogenesis of post-orogenic Cu, Ni-bearing mafic–ultramafic intrusions in Jilin, NE China. J. Asian Earth Sci. 23, 781–797.
Zeng, Q., Qin, K., Liu, J., Li, G., Zhai, M., Chu, S., Guo, Y., 2015. Porphyry molybdenum deposits in the Tianshan-Xingmeng orogenic belt, northern China. Int. J. Earth Sci. 104, 991–1023.
Zeng, Q.D., Liu, J.M., Zhang, Z.L., Chen, W.J., Zhang, W.Q., 2011. Geology geochronology of the Xilamulun molybdenum metallogenic belt in eastern Inner Mongolia, China. Int. J. Earth Sci. 100, 1791–1809.
Zhai, D., Liu, J., 2014. Gold-telluride-sulfide association in the Sandaowanzi epithermal Au-Ag-Te deposit, NE China: implications for phase equilibrium and physicochemical conditions. Miner. Petrol. 108, 853–871.
Zhai, D., Liu, J., Cook, N.J., Wang, X., Yang, Y., Zhang, A., Jiao, Y., 2018a. Mineralogical, textural, sulfur and lead isotope constraints on the origin of Ag-Pb-Zn mineralization at Bianjiadayuan, Inner Mongolia, NE China. Miner. Deposita 1–20. https://doi.org/10.1007/s00126-018-0804-6.
Zhai, D., Liu, J., Ripley, E.M., Wang, J., 2015. Geochronological and He–Ar–S isotopic constraints on the origin of the Sandaowanzi gold-telluride deposit, northeastern China. Lithos 212, 338–352.
Zhai, D., Liu, J., Tombros, S., Williams-Jones, A.E., 2018b. The genesis of the Hashitu porphyry molybdenum deposit, Inner Mongolia, NE China: constraints from mineralogical, fluid inclusion, and multiple isotope (H, O, S, Mo, Pb) studies. Miner. Deposita 53, 377–397.
Zhai, D., Liu, J., Wang, J., Yang, Y., Zhang, H., Wang, X., Zhang, Q., Wang, G., Liu, Z., 2014a. Zircon U-Pb and molybdenite Re-Os geochronology, and whole-rock geochemistry of the Hashitu molybdenum deposit and host granitoids, Inner Mongolia,

NE China. J. Asian Earth Sci. 79, 144–160.
Zhai, D., Liu, J., Zhang, H., Wang, J., Su, L., Yang, X., Wu, S., 2014b. Origin of oscillatory zoned garnets from the Xieertala Fe-Zn skarn deposit, northern China: in situ LA-ICP-MS evidence. Lithos 190, 279–291.
Zhai, D., Liu, J., Zhang, A., Sun, Y., 2017. U-Pb, Re-Os and $^{40}Ar/^{39}Ar$ geochronology of porphyry Sn ± Cu ± Mo and polymetallic (Ag-Pb-Zn-Cu) vein mineralization at Bianjiadayuan, Inner Mongolia, NE China: implications for discrete mineralization events. Econ. Geol. 112, 2041–2059.
Zhai, D., Liu, J., Zhang, H., Yao, M., Wang, J., Yang, Y., 2014c. S-Pb isotopic geochemistry, U-Pb and Re-Os geochronology of the Huangganglang Fe-Sn deposit, Inner Mongolia, NE China. Ore Geol. Rev. 59, 109–122.
Zhang, C., Li, N., 2014. Geology, geochemistry and tectonic setting of the Indosinian Mo deposits in southern Great Hinggan Range, NE China. Geol. J. 49, 537–558.
Zhang, C., Li, N., 2017. Geochronology and zircon Hf isotope geochemistry of granites in the giant Chalukou Mo deposit, NE China: implications for tectonic setting. Ore Geol. Rev. 81, 780–793.
Zhang, J.H., Gao, S., Ge, W.C., Wu, F.Y., Yang, J.H., Wilde, S.A., Li, M., 2010. Geochronology of the Mesozoic volcanic rocks in the Great Xing'an Range, northeastern China: implications for subduction-induced delamination. Chem. Geol. 276, 144–165.
Zhang, J.H., Ge, W.C., Wu, F.Y., Wilde, S.A., Yang, J.H., Liu, X.M., 2008. Large-scale Early Cretaceous volcanic events in the northern Great Xing'an Range, northeastern China. Lithos 102, 138–157.
Zheng, Y.F., 1993. Calculation of oxygen isotope fractionation in anhydrous silicate minerals. Geochim. Cosmochim. Acta 57, 1079.
Zhou, J.B., Wilde, S.A., Zhao, G.C., Han, J., 2017. Nature and assembly of microcontinental blocks within the Paleo-Asian Ocean. Earth-Sci. Rev. 1–18. https://doi.org/10.1016/j.earscirev.2017.01.012.s.